

Sept 9th, 2003

Preliminary comments:

In preparation for this week's meeting at Fermilab we are presenting this first version of a proposal for a scintillator-based detector for the Off-Axis experiment.

Different sections of this draft are the work of several different people. There is some duplication, but essentially all of the material is here, except for the costing, which will appear separately.

The author list includes the work of many people and a final list will be compiled after all have seen the proposal and commented on it.

Section A. Overview

To reach the physics goals described in the previous sections, we propose to build a 50,000 (metric) ton Off-Axis Far Detector. The size of this detector clearly makes its design and construction a substantial challenge. For that reason, we propose to use scintillator for the active detector elements, so that we can rely as much as possible on technology developed and refined for the MINOS Far Detector. We believe that the design, construction and installation of the MINOS Far Detector represents a paradigm that we wish to repeat in this proposed Off-Axis experiment.

While we propose to repeat the MINOS design of alternate layers of scintillator and passive absorber, we also face the challenges of an order of magnitude increase in size and the need for a substantial reduction in detector unit cost. Technology has also advanced in the nearly a decade interval since the MINOS Detector design was developed. For these reasons, we propose to make several modifications to the MINOS design. We propose to achieve both better quantum efficiency and lower cost by replacing the MINOS multi-anode photomultipliers with avalanche photodiodes (APD's). A second change is to use a low-Z, low density absorber, which is better matched to electron identification. The design here replaces the steel absorber in MINOS with wood in the form of inexpensive Oriented Strand Board (OSB). At this point in the detector design, we are still investigating the total cost implications of using mineral-oil based liquid scintillator rather than plastic scintillators used in MINOS. This option is discussed further in the sections below.

The design for the Off-Axis Far Detector is best understood as a combination of three distinct and mostly independent systems—the absorber structure, the active detector

modules and the photodetector with electronics. Although there is some interaction among these systems, to first order, each of these components can be modified separately in order to optimize their performance or minimize their cost without a major impact on the design of the other components.

Absorber Structure: The proposed absorber for the Off-Axis Detector is wood in the form of Oriented Strand Board (OSB). OSB is an engineered wood product, which is low cost and produced in large quantities in the vicinity of the Minnesota end of the NUMI beam. In addition to its properties of low density and low Z, OSB has sufficient structural strength to provide much of the required detector support structure. High efficiency, industrial strength fastening systems, such as quick-set, high-strength adhesives and cartridge-loaded screw guns, exist to install the fasteners required to assemble an OSB structure. The overall Off-Axis Detector design thus incorporates the active scintillator modules into what is functionally a large monolithic block of wood.

Three large factories produce OSB in Northern Minnesota near the proposed sites for the detector, making the on-site assembly of the absorber sub-structure an attractive way to economize on shipping. One of these plants, the Potlatch Oxboard factory in Cook MN is located directly on US Highway 53, the main access road to nearly all feasible Off-Axis detector sites. Our plan for Off-Axis Detector construction is modeled on the successful MINOS experience. The lighter active elements will be manufactured away from the detector laboratory and shipped to the site. The massive quantities of OSB will be produced locally from wood grown and harvested in the vicinity of the detector laboratory. The active elements and the OSB will be combined on-site as the Off-Axis Detector is assembled.

The geometry of the active detector elements is similar to that used in MINOS, but for the Off-Axis Detector, the scintillator strips will be nearly twice as long and are read out only at one end. To take advantage of standard OSB tooling, the Off-Axis Detector will be sized in feet. The Detector cross-section will be 48 feet high by 96 feet wide. Forty eight foot long scintillator modules will be embedded into the OSB structure and arranged to give alternate orthogonal views separated by about 1/3 of a radiation length of absorber. This Detector design and aspect ratio optimizes the fiducial volume of the detector with respect to both cost and ease of construction

The proposed photodetectors are avalanche photo-diodes (APD's) of the type used in the Compact Muon Solenoid (CMS) Detector at the Large Hadron Collider (LHC). They are commercially available in large quantities from Hamamatsu. One APD pixel will be used for each scintillator. APD's have an order of magnitude higher quantum efficiency than the photocathode in photomultiplier tubes (PMT's), hybrid photodiodes (HPD's) or image intensifiers (IIT's), especially for the wavelengths that are less attenuated by a long wavelength shifting fiber. APD's are also significantly less expensive than PMT's or HPD's. APD's are low gain devices. We expect to operate the Off-Axis Detector at an APD gain of 100. This APD gain parameter requires a high gain electronic amplifier, integrated with the necessary shaping, timing, gating, and pulse height measuring circuitry. Such amplifiers have been developed and produced in quantity for silicon strip detectors. To reduce the thermal noise of the APD's, it will be necessary to cool them to approximately 0°F using an electronic Peltier circuit mounted on each APD array. Calculations based on the measured performance of individual elements of the APD, electronics, and cooling systems show that a signal to noise

ratio of about 5:1 is achievable for minimum ionizing particles at the far end of a scintillator strip. Measurements of the entire system noise using existing, but not optimized, electronics are currently in progress.

The active detector modules will be based on those constructed for MINOS using wavelength shifting fiber to transmit the light produced in a long strip of scintillator. Using the same scintillator strip width and thickness as MINOS (4 cm x 1 cm) yields a well documented performance for extruded solid scintillator. Thicker cells (4 cm x 3cm) would reliably give at least the same performance for liquid scintillator at substantially lower cost. The light transmitted down the fiber from the far end would be increased in comparison with MINOS by having a single fiber make two passes through the scintillator with a loop at the bottom. This configuration enables single-ended fiber readout, reducing the number of readout channels, and yielding four times as much light as would be observed from the far end of single fiber. For plastic scintillator, this design requires extruding strips with two grooves, in contrast to the single groove for MINOS. Cost data from the MINOS factories suggest that cost impact of this modification is not large.

The major differences between liquid and solid scintillator is in the construction of the active detector modules. Liquid scintillator has the advantages of lower cost enabling the use of more active and less passive mass, on average more light and the ability to construct the detector with empty, low weight extruded plastic housings, which are filled with scintillator only after the detector is assembled. Solid scintillator benefits from the MINOS experience, which results in lower risk, since the costs and assembly methods are already proven on a large scale using the same core staff that will participate in the Off-Axis experiment.. For that reason,

we discuss both liquid and solid scintillator designs in the following sections.

Section B. Scintillator Detector Simulation

Extensive simulations for the large monolithic scintillator detector have been performed in order to determine the expected signal and background rates, and to determine reconstruction methods that will be useful in analyzing the data optimally

B.1 Simulation framework

The simulations are done using a version of GMINOS, the GEANT based simulation code used for the MINOS detector. This allows the efficient use of some tools that have been developed for implementing and analyzing a scintillator detector. The neutrino interactions are performed by NEUGEN2, which is integrated into the GMINOS code. The output files are ADAMO tables. There were several modifications that were required to correctly implement the photo-detector and proposed strip geometry, and those will be described here.

B.2 Detector Definition

The GMINOS code is designed to efficiently

allow the description of a detector made up of planes of absorber and active detector, with strips oriented along the X or Y axes, and/or at an angle of 45 degrees to these axes. The overall dimensions of the detector, shown in figure 1, are 30m wide, 15m tall, and 162m long. This consists mainly of passive absorber and 900 effective planes of active detector, half with strips oriented along the X axis, and half with strips oriented along the Y axis. The detector that we wish to simulate has a slight difference, in that we would like the active detectors to be located in 2 layers, made of 150cm wide modules alternating in each layer, with no overlap. Figure 2 shows the layout for the X type plane, with strips oriented along the X axis. The individual modules are 15m long with the readout ends located along the outer edges. The hatched areas are filled with absorber, and the open areas indicate scintillator modules for the two layers forming a single plane. Figure 3 shows the layout for the planes with strips oriented along the Y axis. The modules are the same size, and are arranged in two different layers as they are in the X planes.

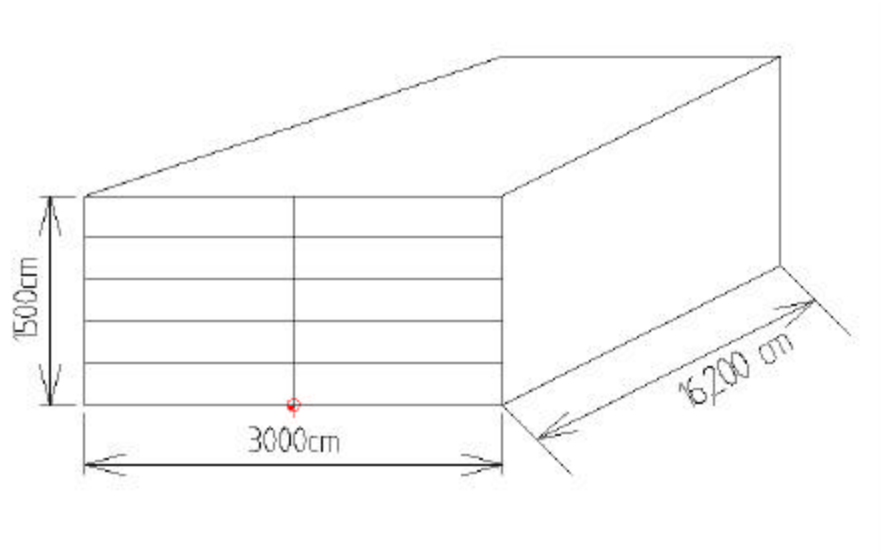


Figure 1 Schematic diagram of the scintillator detector as implemented.

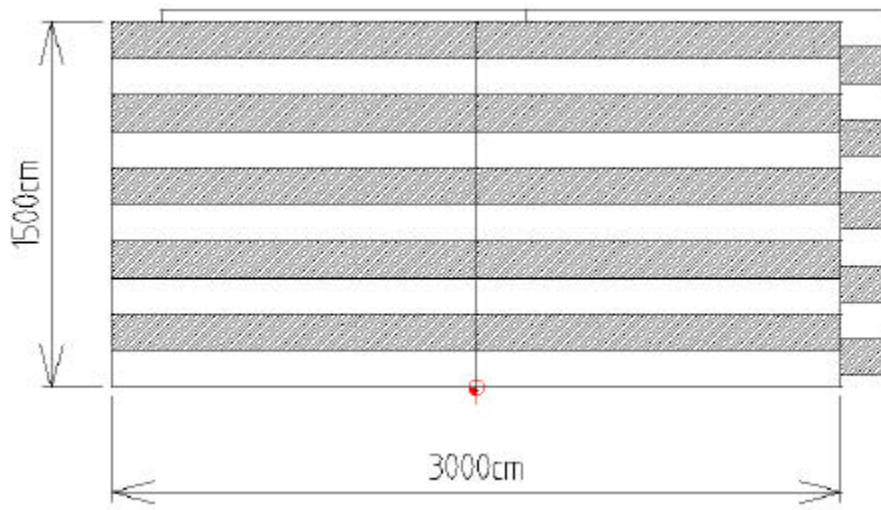


Figure 2 Implementation of modules for X planes, shaded modules are read out in each layer and the unshaded modules are ignored. Each layer is made of 2 15mx15m square sections.

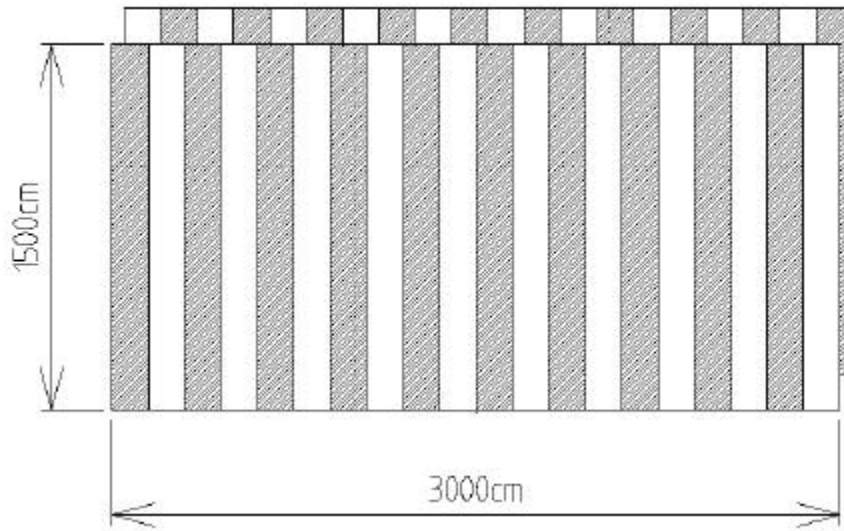


Figure 3 Implementation of modules for the simulated Y axis planes. The shaded modules are read out in each layer, and the unshaded are ignored.

B.3 Simulated plane design

The absorber material was implemented as continuous sheets of a low density Lucite, whose radiation length is very similar to wood, and which will be referred to as wood in this document. The density was decreased in GEANT to 0.7 g/cc to accurately produce the distribution of neutrino interaction vertices. The implementation of the alternating modules in the simulation was implemented as two continuous layers of scintillator modules separated by a one-inch layer of wood. The formulation of the alternating modules was done at the analysis stage rather than generation by logically ignoring any hits in half of each layer as indicated in the figures. The Y-axis planes are straightforward to implement in the GMINOS framework. The first Y-type plane has an absorber with a thickness of 12.5 cm, and an active scintillator plane, and the second Y-type plane has a thin, 2.5 cm absorber and an active scintillator plane.

The X-axis planes have an additional complication in their implementation. These

planes need to have a cut in the middle so that readout of the fibers can be done separately for each side. This was done by implementing each 30 m by 15 m active layer in an X-axis plane as two 15 m by 15 m layers of scintillator. These elements cannot be placed at the same position along the Z direction, so they are placed as close to each other as possible. This has the effect of putting the X axis detectors in the East side of the detector one scintillator module thickness, 1.05 cm, further upstream than the modules on the West half of the detector, where they would actually be coplanar in the proposed detector. In addition, since we want the absorber planes to extend the full width of the detector, they are implemented as their own planes with a zero thickness active plane. In a similar way the active planes are implemented as offset scintillator planes with zero thickness absorber. This means that the X planes are actually implemented as 6 X planes. The first plane is a full width 12.5 cm thick absorber only plane. The second is a scintillator only plane on the $-X$ half of the detector. The third plane is an identical scintillator plane shifted to the $+X$ half of the detector. The

next 3 planes are the same, except that the absorber is only 2.5 cm thick. This makes the numerology of the analysis more complicated since there are 6 X planes and 2 Y planes in a unit cell, but most importantly, it accurately represents the proposed detector.

B.4 Scintillator module design

The scintillator modules themselves were implemented in the same way as the MINOS modules. The width of all of the modules is 300 cm, each containing 75 4 cm wide scintillator strips. As discussed above, these are logically cut in half during the analysis and the top 38 or bottom 37 strips of each module are read out from the consecutive layers along the Z-axis. The strips themselves are 1 cm thick in total with a dead layer of 0.25 mm on all sides made of TiO₂ loaded polystyrene, as in the actual strips. The outer skins of the modules were implemented as 0.25 mm iron, to match the desired material.

B.5 Simulation plan and status

Several types of interactions were simulated, spanning the range of energies, neutrino types and interactions. The neutrino interactions were chosen with a 1/E energy distribution so that the interacted neutrino spectrum is approximately flat in 2 energy ranges: a low energy range from 100 MeV to 3 GeV, and a high energy range spanning 3 GeV to 20 GeV. Data sets were generated for the charged current interactions of both electron and muon neutrinos and antineutrinos. The neutral current interactions were simulated for muon neutrinos and antineutrinos. The distribution of the 2.1 million simulated neutrino events is shown in the following table. The emphasis was placed on the muon neutrinos, as the low energy muon neutrino charged current interactions are a significant background when the muon track is not obvious. The neutral currents are also emphasized, as they too are a significant background that must be strongly suppressed by the analysis.

ν_μ CC	$\bar{\nu}_m$ CC	ν_e CC	$\bar{\nu}_e$ CC	ν_μ NC
600,000	300,000	300,000	300,000	600,000

B.6 Analysis of Sensitivity to $\nu_m \rightarrow \nu_e$ Oscillations

We have performed an analysis of the events described above, in order to determine the sensitivity of the scintillator-based detector to $\nu_m \rightarrow \nu_e$ oscillations. First, the events were weighted according to the off-axis beam spectrum, assuming the detector to be located 732 km from the neutrino source and 10 km off-axis. The events were then normalized assuming a 5-year exposure of the 50 kT detector and a proton intensity of 4e20 protons on target per year. The

resulting energy spectra are shown in figure 4.

The ν_μ CC sample was oscillated with parameters $\Delta m^2 = 2.5\text{E-}3\text{eV}^2$, $\sin^2(2\theta) = 1$ and the ν_e sample was oscillated with $\sin^2(2\theta_{13}) = 0.1$ (the CHOOZ limit). The events were divided into two equal samples of 280,000 CC events, 280,000 NC events and 120,000 ν_e events. One sample was used as a training sample to define cuts and generate probability density functions and the other sample was used to determine the final selection efficiencies.

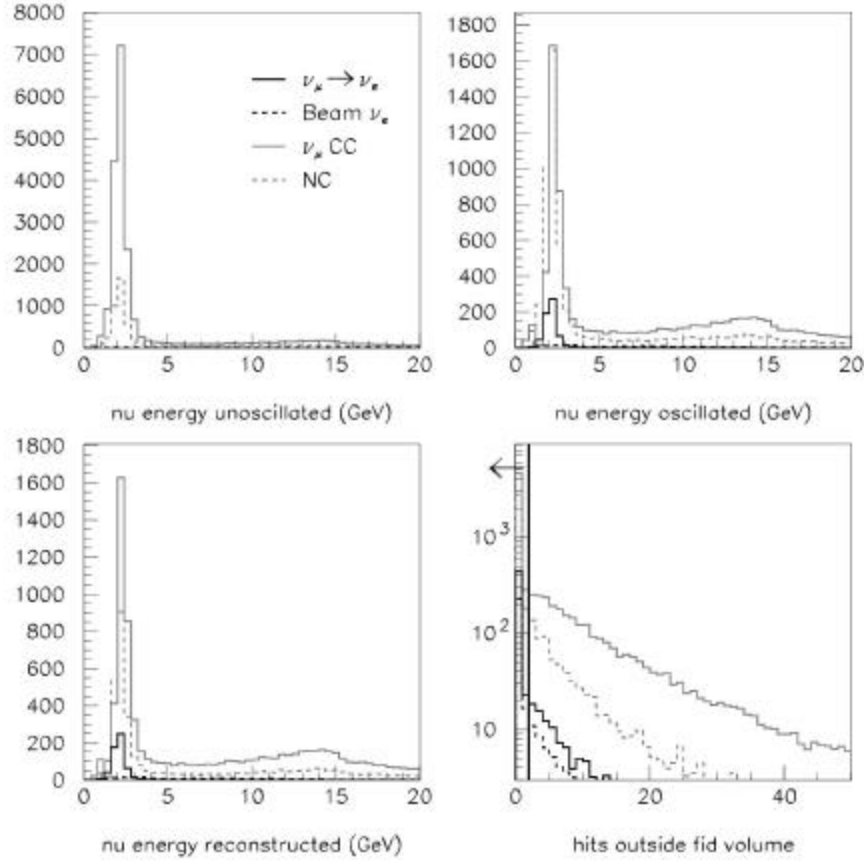


Figure 4 Event samples used in this analysis. Top left: unoscillated true neutrino energy distributions. Top right: oscillated energy distributions. Bottom left: energy distributions for events that form a valid cluster. Bottom right: distributions of numbers of hits outside the fiducial volume of the detector. Events with more than 2 hits outside the fiducial volume are rejected.

A loose clustering algorithm was applied to the events that grouped together hits in each view occurring within a distance of 2m of each other. A minimum of three hits in each view was required. This removed outlying hits from events and rejected low energy (chiefly neutral current) events. Events with more than two hits outside the fiducial volume of the detector (50 cm in x and y and 2 m in z) were rejected at this stage. 84% of the ν_e events passed this fiducial requirement.

A straight line was fitted to the clusters in each view and the hit and pulse height residuals were calculated. The clusters were

then passed through a filter that used the Hough Transform to select the most significant track-like segment of each event. This filter is an iterative procedure where the 2-dimensional hits (x_i, y_i) in the cluster are transformed into trajectories in the parameter space (\tilde{n}, d) where the relation $x_i \cos \tilde{n} + y_i \sin \tilde{n} - d = 0$ is asserted. The parameters of the most significant track-like segment of the event were taken to be those where the peak in (\tilde{n}, d) space occurs, and the hits belonging to the track were those whose trajectories passed within a preset minimum distance to this peak. The procedure was repeated with finer binning in (\tilde{n}, d) space and more stringent cuts on the minimum

distance to the peak. Figure 5 illustrates the effect of the filter for sample ν_μ CC, NC and ν_e events. In this implementation, electron showers tend to be sufficiently narrow that

most of the shower hits were included in the track-like object, whereas fewer hits were tagged as track-like for NC showers, which are generally more diffuse.

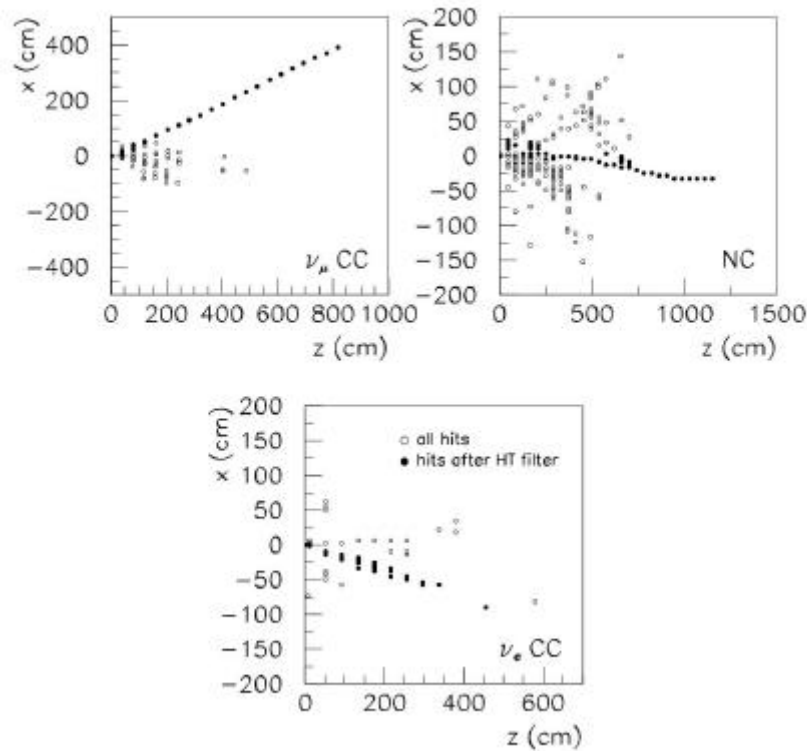


Figure 5 Use of the Hough Transform filter on three example events. The open circles show all the hits in the event and the filled circles show the hits that remain after the filter is applied.

Several cuts were then applied to the events to provide initial rejection of CC and NC events:

- $200 < \text{event length} < 700 \text{ cm}$ (rejects long muon tracks and short NC events)
- $8000 < \text{total pulse height} < 18000 \text{ pe}$ (rejects low-y NC events)
- minimum gap between hits in either view > 3 logical planes
 - (effectively a single missed plane -- rejects track-like events)
- fraction of hits found by Hough Transform > 0.7 (preferentially selects low-y ν_e CC events)

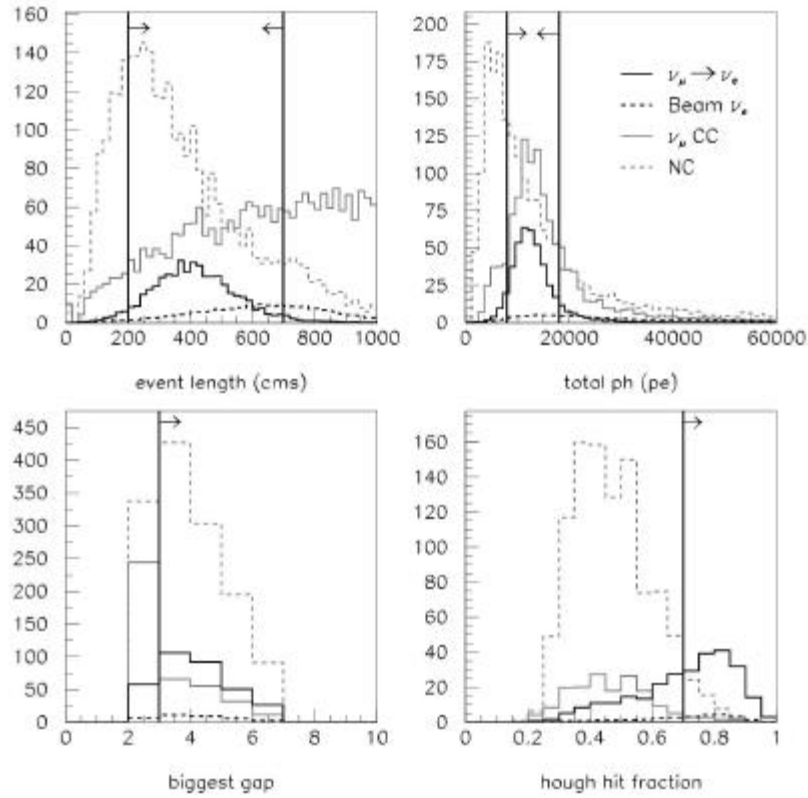


Figure 6 Distributions of event length, summed pulse height, the minimum gap (in planes) between hits in the event and the fraction of hits in the event found by the Hough Transform filter. Note that due to the numbering scheme of active scintillator planes in the simulation, the minimum gap between successive planes is 2. The cuts are applied in the sequence top-left to bottom right in this figure.

Distributions of these quantities and the locations of the cuts are shown in figure 6. A likelihood analysis was then performed on the remaining events, using the following variables:

1. number of hits in view with minimum number of hits
2. event length
3. minimum gap in event
4. pulse height vs. pulse height weighted residual
5. hits per plane vs. pulse height per plane
6. total number of planes
7. pulse height residual for hits selected by Hough Transform (HT)
8. pulse height per plane for hits selected by HT
9. fraction of hits selected by HT
10. fraction of pulse height selected by HT
11. total pulse height selected by HT

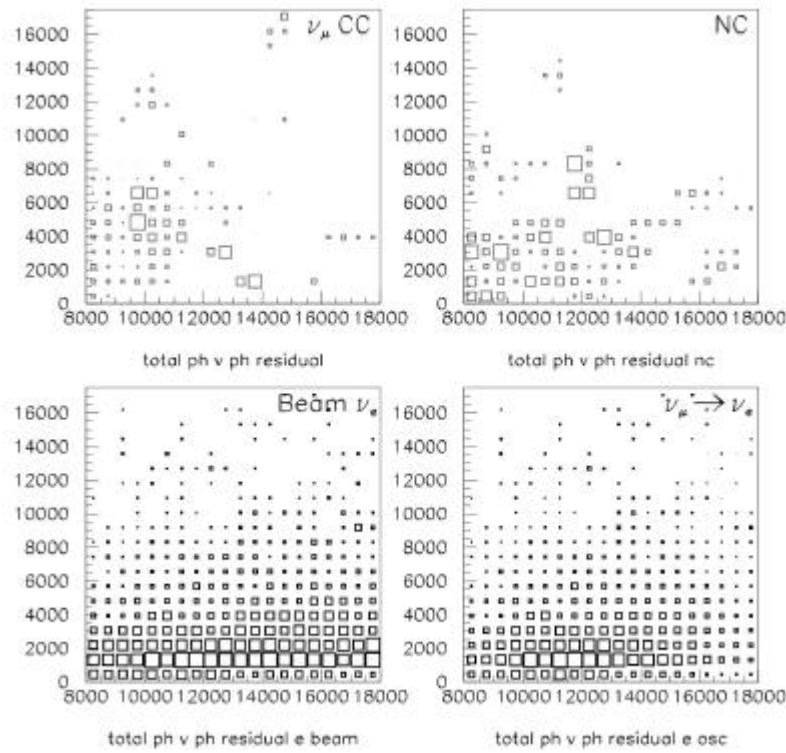


Figure 7 Total pulse height versus pulse height residual distributions.

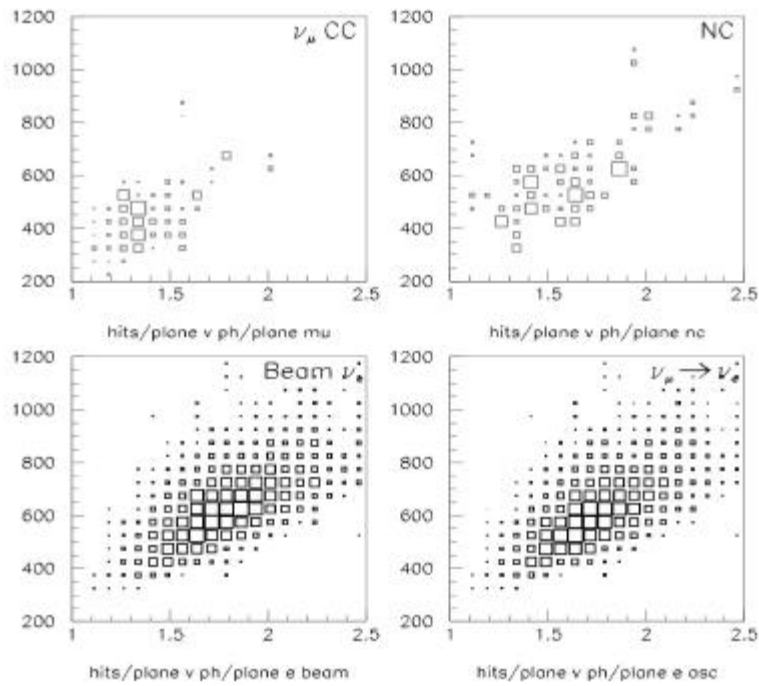


Figure 8 Hits per plane versus pulse height per plane distributions.

Distributions of these variables are shown in figures 7-9. Log likelihood ratios were formed from the product of the individual probability distributions, for an event to be classified as either ν_e signal or CC, NC, beam ν_e background respectively. These likelihood ratios are shown in figure 10. There is good discrimination between ν_e

signal events and neutral current and charged-current backgrounds. There is less separation between ν_e signal events and beam ν_e background; here the only discrimination is that the beam ν_e events tend to be of higher energy than the $\bar{\nu}_m \rightarrow \bar{\nu}_e$ signal.

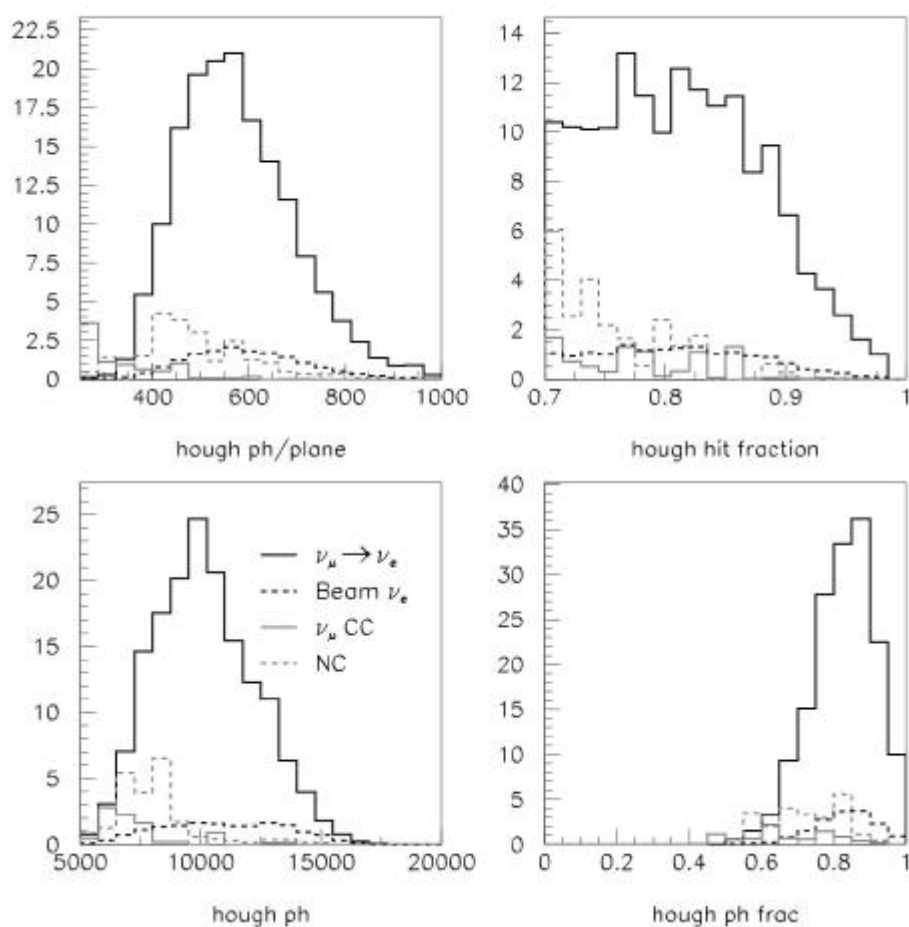


Figure 9 Distributions derived from hits selected by the Hough Transform (HT) filter. Top left: pulse height per plane. Top-right: fraction of hits selected by HT filter over the total number of hits in the event. Bottom-left: summed pulse height. Bottom-right: fraction of the total event pulse height in the hits selected by the HT filter.

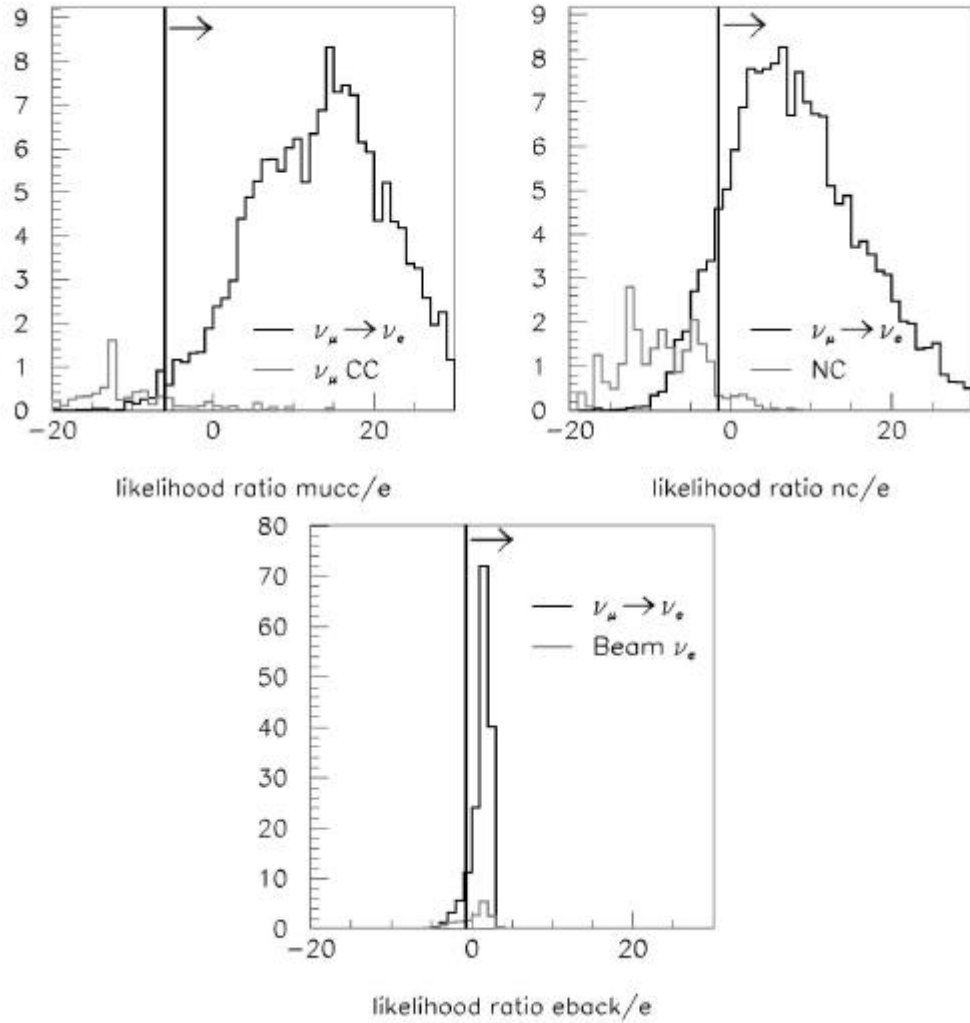


Figure 10 Log likelihood ratio distributions for the various event classes.

The following cuts on the likelihood ratios define the sample of ν_e events in this analysis:

$$\log L_{e/\hat{1}} > -6, \log L_{e/NC} > -1.5, \log L_{e/ebeam} > -0.75$$

These cuts on these likelihood ratios were optimized using the first of the two event samples, and were selected in order to maximize the ratio of the number of signal

ν_e events to the square root of the total number of background events. The distributions shown here show the result of applying the selection cuts to the second, independent, sample of events. Table 1 shows the breakdown of the event types in this second sample, and the effect of the various cuts on these events.

Table 1 Breakdown of the cuts and efficiencies for the event samples used in this analysis.

Cut	ν_μ CC	NC	beam ν_e	$n_m \rightarrow n_e$ signal
generated events	279944.0	252901.0	119960.0	119960.0
beam weighted	26898.5	7601.5	471.9	26079.7
beam weighted +osc	10328.6	7601.5	471.9	796.5
reconstructed events	9930.2	4693.5	424.0	728.0
fiducial volume	6626.6	3941.9	326.7	612.7
event length	1530.5	2519.2	177.5	549.6
total ph	930.7	911.3	48.1	453.4
total planes	526.2	740.7	43.3	420.7
gap	217.2	555.8	35.5	347.6
hough fraction	12.7	29.9	20.4	202.6
likelihood	0.9	1.5	13.2	163.2

Defining the figure of merit as the number of $n_m \rightarrow n_e$ signal events divided by the square root of the total number of background (ν_μ CC, NC and beam ν_e) events, the following results are obtained:

lower figures of merit, typically in the range 35-40.

- signal=163.2 events,
background=15.6 events
- figure of merit=41.3
- ν_e efficiency=20.5%
- ν_μ CC rejection=1E-4
- NC rejection=2E-4

Using these cuts, the background due to misidentified ν_μ CC and NC events is reduced to a level that is an order of magnitude below the intrinsic beam ν_e background. It seems difficult to reduce this background further, since the only difference between beam ν_e and signal $n_m \rightarrow n_e$ events is the energy distribution, and this is already taken into account by including the total pulse height distributions in the likelihood analysis. The cuts listed above appear to be optimal; we have investigated other potential optimizations where the cuts on the likelihood ratio and Hough hit fraction are relaxed in order to increase the $n_m \rightarrow n_e$ selection efficiency, and found that these tend to yield somewhat

Section C. Solid Scintillation Detector

C.1 Introduction: Our design for the solid scintillation detector modules is based upon our considerable experience with the design and manufacture of the detector modules for MINOS. The design presented here uses plastic scintillator as the detection medium, for which we are able to provide quite accurate estimates of production costs. However, we also carried out considerable research and development for a liquid scintillator based detector for MINOS [1] and we will present a liquid scintillator option for the current detector in Section Y.X. The choice of liquid would provide significant cost reduction in terms of both material and manufacturing with only slight modification of the overall construction plan.

The MINOS plastic scintillator is a conventional polystyrene-based scintillator doped with PPO and POPOP fluors, and extruded in 4.1 cm wide by 1.0 cm thick strips with lengths up to 8 m [2]. An integral part of these strips is a co-extruded 0.5 mm thick outer layer of titanium dioxide loaded polystyrene, which provides a highly efficient reflector for the blue scintillation light. After several reflections, typically, this blue light hits a 1.2 mm diameter wavelength-shifting (WLS) fiber glued into a groove in the scintillator strip, where it may be absorbed and then re-emitted as green light. The WLS fiber acts as a light-guide to carry the green light to an external photo-detector. Figure 1 is a photograph of a MINOS module during manufacture.

In the liquid scintillator version of this detector, the liquid scintillator would be held inside multi-cell extrusions of polyvinyl-chloride (PVC) containing 10-15% titanium dioxide. The cells would be thicker than the solid scintillator strips along the beam

direction, to make up for the lower scintillation light-yield of the liquid.



Figure 11 A MINOS module during manufacture. The green WLS fibers have been glued into grooves in the scintillator and guided via a manifold to an optical connector. The top of the module remains to be attached, and the fiber ends fly-cut.

A scintillator *module* for the Off-Axis Detector would be 4 ft wide, commensurate with the OSB-board absorber dimensions, and would contain 30 individual scintillator strips (or PVC cells) each 4.0 cm wide. At the ends of the module, a manifold guides all WLS fiber to a single optical connector, where a pixelated photo-detector is located.

A crucial parameter for this detector is the maximum possible length of a module; this determines the overall detector dimensions and is an important cost-driver. We plan to make modules that are 48 ft in length (14.4 m) corresponding to the length of the basic absorber panels used in the construction. This is almost twice the length of the MINOS modules. The critical quantity that determines the maximum length of is the light yield from the far end of a WLS fiber. For a given light yield in the scintillator and for maximum reflectivity of the walls of the scintillator, this is determined by the

attenuation properties of the WLS fiber, coupled with its diameter. We will discuss this in detail.

Another key element of our design is the introduction of avalanche photodiodes (APD's) as the photo-detector elements. These have two advantages over photomultiplier tubes (PMT's) as used in MINOS, provided their noise level can be kept sufficiently low: high quantum efficiency and low cost. The cost per channel in bare die form in the quantities appropriate for this experiment (600,000) is \$2.70 per channel, to be compared with a cost of about \$12 for similar quantities of multi-channel PMT's. The APD quantum efficiency is 85% in the wavelength region of interest vs 10% for a PMT with bi-alkali photocathode.

Since the APD is a relatively new photo-detector, we will include a general discussion of its operation, plus the CMS experience with large numbers of the devices.

C2. Design parameters of the scintillator/WLS fiber system

The required light yield. As described earlier, a major development in photo-detection has occurred since the MINOS detectors were designed: the production of inexpensive, pixelated, avalanche photo-detectors (APD's) by Hamamatsu. These provide an essential

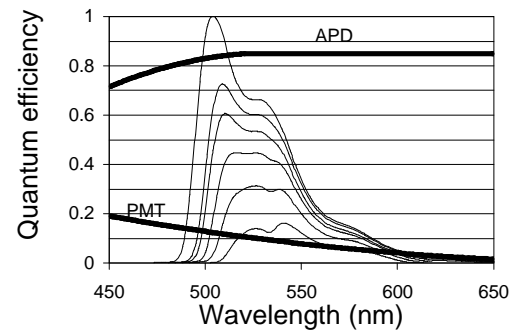


Figure 12. Quantum efficiencies of APD and PMT (bi-alkali photocathode) as a function of wavelength. The figure also shows WLS fiber emission spectra measured at lengths of 0.5, 1, 2, 4, 8, 16 m, respectively and illustrates the shift of the average emission wavelength as attenuation (fiber length) increases.

component in our ability to make affordable, very long scintillator modules with sufficient light yield from the end remote from the photo-detector.

Figure 2 shows the quantum efficiency of the APD along with that of the PMT used in the MINOS detectors: 85% vs 10% at the relevant wavelengths. The figure also shows emission spectra measured at the ends of different lengths of WLS fiber. This illustrates another advantage of the APD: its quantum efficiency increases at longer wavelengths, as does the average wavelength of emission, while that of the PMT falls. This leads to a longer effective attenuation length for light in the fiber, as shown in figure 3, where the attenuation data were obtained using a Hamamatsu APD of the type we intend to use, and a Hamamatsu M-16 PMT as used in MINOS.

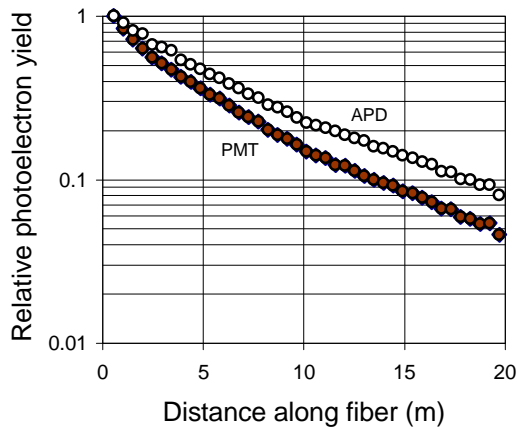


Figure 13. Relative photoelectron yield from 1.2 mm diameter WLS fiber, for APD and PMT. The data have been normalized at 0.5 m to illustrate the effect of the longer wavelength response of the APD

We consider 48 ft (14.4 m) to be a suitable figure for the length of a scintillator module; this is a length that can be easily shipped by road, and which corresponds to absorber dimensions easily constructed from standard materials.

In a later section, where we discuss APD performance in more detail, we will show that a signal of 30 photons will produce a signal/noise ratio of greater than 5:1, sufficiently far above the noise level to unambiguously determine the light signal from the far end of a WLS fiber. Consequently, we use the criterion that we must achieve a light yield of 30 photons/minimum ionizing particle (mip) from the far end of a 14.4 m long scintillator module and the following section will describe how this will be achieved.

Optimization of the light yield: The expected light yield and uniformity of the scintillator and wavelength shifting (WLS) fiber system are derived from both measurement and calculation, and from our experience with the 8-m long MINOS modules.

The main factors that affect the light yield of the system are: the geometry of the scintillator strips, the composition of the co-extruded TiO_2 layer, and the diameter, position, and configuration of the WLS fiber. Following the MINOS experience, we would like to change as few of these parameters as possible. However, since the length of the strips we wish to use is almost twice that of the MINOS detector, some changes are necessary to achieve reliably detectable light levels. Since the signal is smallest at the far end of the strip, most of the calculations will be concerned with the signal from the far end.

The scintillator strips themselves will change very little: they will be longer, and slightly narrower, 4.0 cm vs. 4.1 cm, in order to fit in the module packaging. However, the strips will remain 1.0 cm thick along the beam direction. The co-extruded layer, which provides the reflective walls, will be of the same composition and thickness as the MINOS strips.

Measurements in the installed MINOS detector show that the average light output at the center of a strip, 4 m from the end, is 4.25 photoelectrons per minimum ionizing particle (*pe/mip*). (The actual measured level, shown in figure 4, is higher than this because of the relativistic rise in energy loss of the higher energy underground muons). Since the average quantum efficiency of the PMT bialkali photocathode is 0.10 for the fiber emission spectrum at this position, we conclude that there are 43 *photons/mip* collected from this point.

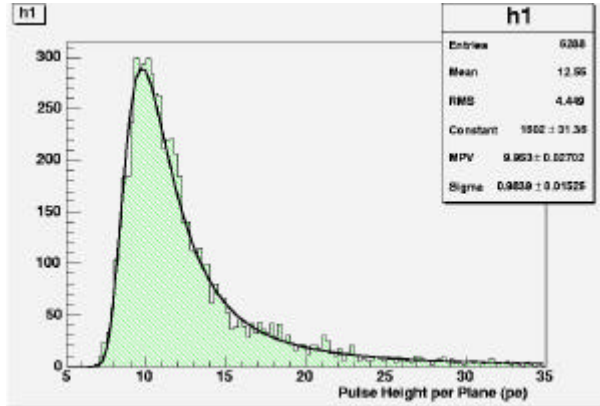


Figure 14. Pulse height distribution of underground muons in MINOS scintillator strips. The data correspond to the summed signal from both ends of the strip; they have been corrected for track length and normalized to the center of a strip, 4 m from the end. The solid curve is a Landau distribution.

From the attenuation data shown in Figure 3, the relative attenuation factor for the APD between the 4 m calibration point of MINOS modules and the 14.4 m distance is a factor 0.28, giving a light yield of 12 *photons/mip* in the MINOS strip configuration, with 1.2 mm diameter WLS fiber. If we were to install a simple mirror on the end, as was done for the MINOS Near Detector modules we can achieve a 70% increase in the light level to 20 *pe/mip* in the APD, too low for efficient detection.

There are several possible ways to increase the signal level. One is to increase the diameter of the WLS fiber, since, as shown in figure 5, the light output is roughly proportional to diameter. (Our measurements also show that the attenuation properties of the fiber are independent of fiber diameter). However, one problem is that the fiber manufacturer, Kuraray, are unable to supply fiber much thicker than

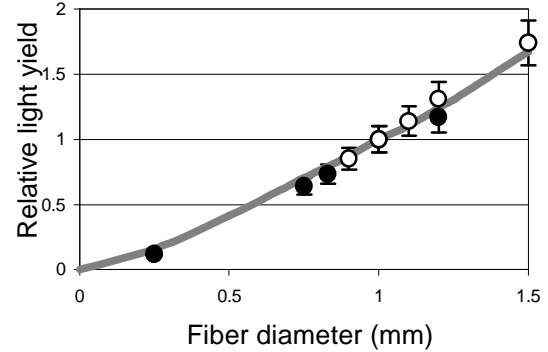


Figure 5. Relative light yield as a function of WLS fiber diameter. Open circles - from NuMI note-212; closed circles - recent measurements; solid line - Monte Carlo simulation. (Data are normalized to unity at 1 mm diameter)

1.2 mm in a spooled format because it becomes too stiff and prone to damage. That would make shipping and construction of such long strips nearly impossible. Second, the price of fiber is nearly proportional to volume, so the overall cost goes as the square of diameter, approximately.

In order to increase the light yield (and optimize the cost) we propose to use *two thinner* fibers, each 0.8 mm diameter, glued into two grooves in the scintillator. However, rather than being two separate fibers, this would actually be a single fiber with a loop at the far end, and with the two near-ends going to a single photo-detector pixel. This looped fiber configuration reduces fiber cost significantly. In addition, the loop acts like a perfect mirror, which actually doubles the light output from the far end. A looped 0.8mm fiber will give 32 *photons/mip* from 14.4 m.

The looped fiber gives another benefit over a mirrored single fiber: it reduces the variation in signal along the length of the WLS fiber. Figure 6 shows the attenuation curve for a single fiber vs a looped fiber; the ratio of

near/far signals is 8 for a single fiber, while for a looped fiber the ratio is only 4.

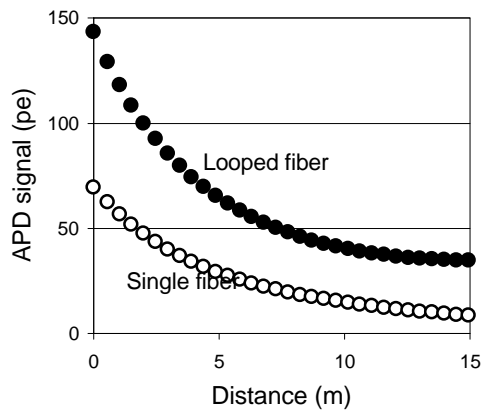


Figure 6. APD signal for looped and single 0.8 mm diameter fiber

C3. Manufacturing the scintillator modules.

Solid scintillator. Over 4,000 scintillator modules were made for the MINOS Far Detector at two separate factories, one at Caltech and one at Minnesota. The factories took delivery of extruded scintillator strips, formed them into multi-strip modules, glued in WLS fibers, enclosed them between aluminum covers, and attached manifolds and optical connectors. Each module was then mapped at 8 cm intervals along each strip using a 5mCi ^{137}Cs γ -source, and the data entered into a database. These factories each operated one shift for almost exactly two years.

Based on our MINOS experience, there are obvious ways to achieve significant reduction in construction costs, both in materials and by using more mechanization.

Liquid scintillator. The principal difference from the solid scintillator detector is that the factories would only be required to insert the looped WLS fiber into PVC multicell extrusions, attach manifolds and optical

connectors, seal the whole module, and test for fiber continuity and leaks, using pressurized gas. Liquid scintillator would only be added once the modules are incorporated into the actual detector. These factory operations are much less complex than for the solid scintillator and could be achieved in a correspondingly shorter time.

Section D. A liquid scintillator option for the Off-Axis detector

OVERVIEW: Liquid scintillator technology is well understood. It has been used for many years for detectors at both accelerators and underground. For physics measurements, liquid scintillator detector offers the same advantages as solid scintillator.

The design considerations presented here are derived from an extensive R&D program we carried out to develop a liquid-based detector for MINOS[ref].

For the Off-Axis detector, we propose to use 14.4 m (48 ft) long multicell extrusions of PVC, each containing 32 cells of width 3.75 cm, the same dimension transverse to the beam that we proposed for the solid scintillator. However, the cells would be 3 cm thick along the beam direction, to compensate for the lower light yield of the liquid. All other considerations would be the same as for the solid detector, i.e. WLS fiber dimensions, photo-detector type. Some slight modification would be made to accommodate the thicker detector modules inside the wood-based absorber.

The distinguishing feature of a liquid detector is its simplicity; this has major implications, not only for cost, but also for construction and maintenance. We enumerate some of the advantages below:

Ease of construction: The liquid scintillator detector is assembled from a few, very simple components. The multicell extrusions are delivered from the extruder already cut to length and possibly sealed at one end. Assembly of a module then consists of inserting a looped fiber into each cell and gluing an end-cap to one end of the extrusion (if not delivered sealed) and a manifold/optical connector assembly at the other end. There are no critical tolerances:

the positioning of the fiber in the cells is not critical.

Reliability: It is easy to check the quality of individual components, i.e. fibers and extrusions, both before and after assembly. Before assembly, all WLS fibers would be subjected to the rigorous checks developed for the MINOS detector. After assembly, a simple device that connects to the optical connector on a module will provide a final check for fiber continuity. A pressure test will verify the integrity of the seals at both ends of the detector.

Ease of shipping: We will likely adopt the MINOS procedure of assembling modules at universities. Liquid scintillator modules will then be shipped empty to the detector laboratory. The low weight and of such modules makes shipping easier and less costly. Tests we have made on similar modules show low sensitivity to vibration. Nonetheless, we expect to adopt the MINOS procedure of initially re-testing all modules upon delivery at the detector laboratory and prior to installation, at least until we develop expectations about the condition of modules at delivery. We expect a repeat of the MINOS finding that visual inspection and minimal testing is all that is needed to eliminate shipping damage.

Ease of installation: There are no fragile parts. Modules will be mounted directly into the wood-based absorber modules and *filled with scintillator only after installation*. Because the modules are light in weight, they can be individually handled by installation workers with standard rigging equipment or cranes.

Ease of maintenance: Once the cells have been filled with scintillator, essentially no maintenance is required. If a module should develop a leak, the liquid scintillator can be pumped from the module and an attempt will be made to seal the leak using standard leak-sealing technology.

D.2 Nominal Design Parameters.

PVC cells:

- 120 cm wide extrusions/32 cells each
- 14.4 m length
- 3.75 cm cell width
- 1 mm inner wall thickness
- 2 mm outer wall thickness

Scintillator:

Bicron 517L, mineral oil based
(added after installation).

WLS fibers:

0.8 mm diameter multiclad fibers,
same as for solid scintillator.

D.3 Light yields

As part of our MINOS R&D, we measured light yields in many 8 m long samples, using cosmic rays and a variety of photo-detectors. All such measurements, and the tests to be described in the following sections, were made with “off-the-shelf” extrusions that have 2.1 cm thick \times 2.8 wide cm square cells. The reflectivity of these cells is significantly lower than optimal (94% vs 96.5% which can be achieved by optimizing the TiO_2 concentration), but their immediate availability was a very large advantage.

We showed that the light yield is well understood and we are able to calculate absolute yields that agree with measurements. In the process of the MINOS design effort, it has demonstrated that the yield is a multiplicative combination of the scintillator response, the reflectivity of the plastic, and the response and attenuation of the fiber. This means that the response of a module can be completely determined by individually testing the components before

assembly, with obvious cost saving implications. Specifically, the determining factors are:

Scintillator: Bicron BC517L scintillator was chosen because it is completely benign; no evidence for its interaction with either PVC, adhesives, or WLS fibers has been seen. (This will be discussed in a later section). It has a lower light yield than some liquid scintillators, but our tests have shown that high light yield is generally associated with chemical reactivity. Figure 1 shows some light yield measurements of BC517L, compared with that of the MINOS extruded plastic scintillator. The “fresh BC517L” is actually an identical formulation of Eljen 321 and shows that the light yield is 75% that of the MINOS scintillator. The “old” BC517L is a sample that has been stored in a plastic container for over 5 years and shows the effect of oxygenation of the scintillator, namely a loss of $\sim 30\%$, which actually occurs in a short time period. Oxygenation is reversible by bubbling nitrogen gas through the scintillator, but we have no plans to do it in the detector.

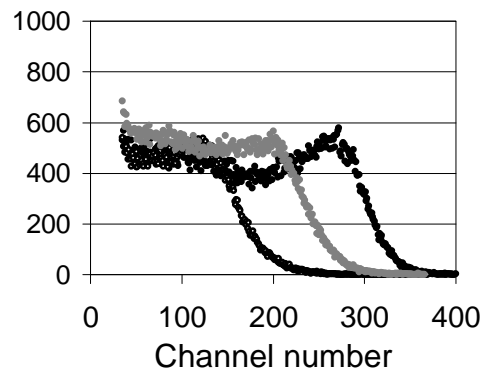


Figure 15. Pulse-height spectra of scintillators showing Compton edge of Cs137 gammas. Black circles: MINOS scintillator; gray: fresh BC517L; open 5-year old BC517L

We have measured the emission spectrum of BC517 and other liquid scintillators; they are

very similar to the MINOS scintillator and provide a good match (Stokes' shift) to the absorption spectrum of the WLS fibers.

Reflectivity of the PVC walls: We obtained many 5 cm × 10 cm samples from a color house and measured the reflectivity of each as a function of wavelength and TiO₂ concentration. A maximum reflectivity of 96.5% at 425 nm was obtained with 10 to 15% TiO₂ (as eventually used for the reflecting cap on the MINOS plastic scintillator extrusions).

Figure 2 shows the emission spectrum of BC517L along with measured optimal reflectivity. The rapid fall in reflectivity below 400 nm is characteristic of TiO₂.

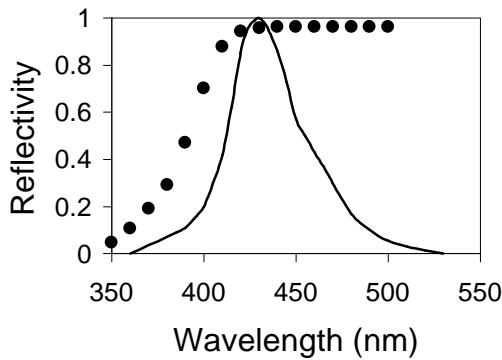


Figure 16. Maximum reflectivity of PVC sample (black circles); the solid line is the emission spectrum of BC517L.

Cell geometry, or specifically the ratio of fiber diameter to average cell dimension: This effect has been extensively simulated and measured. A very important feature is that the yield depends only slightly on the actual position of the fiber in the cell; the yield falls by 20% when the fiber is situated in the corner of the cell as opposed to the center (assuming that the corners are slightly rounded, as they are in actual extrusions, and not perfectly square). Some simulation results are shown in Figure 3, below.

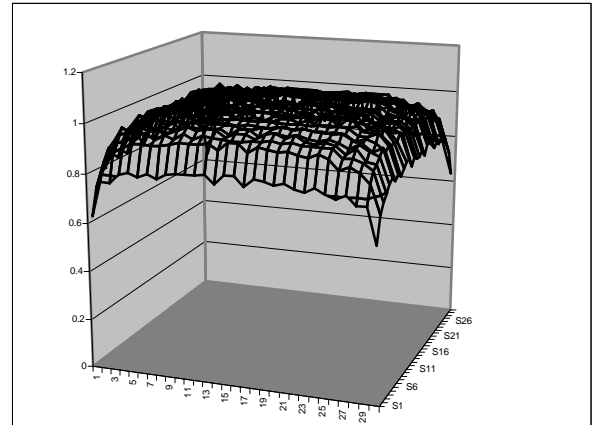


Figure 17. Relative light yield as a function of fiber position in cell.

Figure 4 shows a pulse height spectrum due to cosmic ray muons, obtained from 7.5 m along one of the “off-the shelf” extrusions with 94% reflectivity, using a hybrid photodiode detector with a quantum efficiency of 12%. From our simulations, we can deduce that this pulse height corresponds to a relative light output of 0.75 times that of the MINOS scintillator, in satisfactory agreement with the data shown in Figure 1.

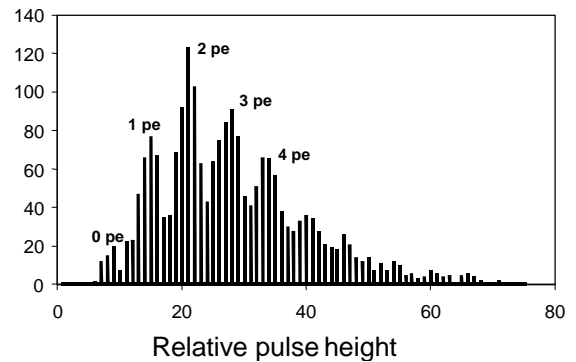


Figure 18. Pulse height spectrum of cosmic ray muons at 7.5 m distance; 2.1 cm x 2.8 cm cell; 1.0 mm WLS fiber; HPD photodetector,

Using our simulations, we are able to estimate the photon yield from muons

passing near the end of a 14.4 m cell as a function of both cell thickness and WLS fiber diameter. We assume that we will use a looped fiber, that the width of the cell is 3.75 cm, that the cell walls have the same reflectivity as the MINOS solid scintillator, and that the fully oxygenated BC517L has a light output of 0.50 relative to the MINOS scintillator. The results are shown in Table 1.

Table 2. Number of photons from 14.4 m as a function of cell thickness and WLS fiber diameter

	2.0 cm	2.5 cm	3.0 cm
1.0 mm	42.8	50.4	56.0
0.9 mm	37.2	43.8	48.7
0.8 mm	31.7	37.3	41.4
0.7 mm	26.1	30.7	34.2

We conclude that a cell thickness of 3.0 cm and a WLS fiber of 0.8 mm diameter will provide the necessary light yield.

D4. Possible aging and lifetime issues; seal integrity

We have performed numerous tests using elevated temperatures and pressures to test the robustness of the detector:

Scintillator/PVC interaction. A series of tests show no measurable effect of long-term, high ambient temperature exposure of PVC to scintillator, either on the PVC or the scintillator.

Creep tests: We measured the physical dimensions of test modules (8 cell by 30 cm long) filled with scintillator under 25 psi constant pressure and at temperatures of 35 and 50°C for periods up to 6 months. (The maximum hydrostatic pressure in the Off Axis installation would be 14 psi). No change in dimensions beyond what is predicted from elastic behavior was seen; these are displacements of 0.3 mm maximum, at the center of a cell.

Elastic modulus of PVC: We measured the deflection under various loads of strips of

PVC maintained in scintillator at a temperature of 50°C for up to 3 months. No change in the modulus was observed, to 5% accuracy.

Light yield tests: Sealed glass vials of scintillator containing PVC and PVC cement samples were held at temperatures of 35 and 50°C. Light yield was measured using a Compton edge from a radioactive gamma source. No change (<3%) was observed up to 6 months.

Scintillator/fiber interaction: We made a number of measurements to check on possible long-term liquid scintillator-WLS fiber interaction. We found no effect based on the following studies:

Single-clad fibers were kept in scintillator at room temperature for more than 2 years; these would be much more susceptible to interaction than the multiclاد, which have a tough polyfluor outer cladding. There was no observed effect on either core or cladding.

100 m of multiclاد fiber was kept in scintillator at 50°C for over 6 months. There was no observed effect.

The core of a multiclاد fiber, with the cladding sanded off, was kept in BC517L for 1 year with no observed effect.

A prototype electromagnetic calorimeter (built by R.Rusack et al. for COSMOS) gave the same pulse height for through-going muons after 2.5 years. This contained 256 single-clad fibers, each 0.56 m long, in 517L scintillator.

A previous paper by other authors estimated the lifetime of single-clad fibers as >15 years in BC517L scintillator.

(Rad.Phys.Chem., Vol 41, 215 (1993))

End-cap and manifold seals: Our evaluation studies of the seals between the extrusion and the endcap at one end and the extrusion and the manifold at the other end show both seals to be rugged and reliable. The joints we glued with ``Weld-On #719" PVC pipe cement. 30 test modules (8 cell, 30

cm long) were built, all with end-caps, (some with bypasses for the MINOS detector).

They were subjected to a variety of tests to determine ultimate strength:

(a) **Burst tests:** The extrusions burst at 100 psi, typically. There were no end-cap or bypass leaks at up to 10 times the expected hydrostatic pressure. High (50°C) or low (20°C) temperatures do not affect this result.

(b) **Impact tests:** Steel rods dropped on end-caps and bypasses had no effect at up to 73 ft-lb (at room temp and at -20°C).

(c) **Thermal and pressure cycling:** No observable effect after repeated thermal and pressure cycling.

(d) **Vibration:** No observable effect.

D5 Engineering; construction and installation.

Considerable engineering effort went into the design of the liquid scintillator alternative for MINOS, and much of that effort carries over directly to the Off-Axis detector. Two Mechanical Engineering Masters degrees were awarded for some of this work, and many of the engineering details are described there [refs].

Module manufacture. There are three operations involved in making modules: fiber insertion, end-cap attachment, and manifold attachment.

(a) **Fiber insertion:** A machine for automatic insertion of fibers was designed; it would have to be modified for insertion of the looped fiber.

(b) **End-cap attachment:** Many end-caps were glued and tested, as described in the previous section; they proved to be very rugged. The seal actually just seals the outer edges of the module; the cells are connected at the far end so that liquid can flow between cells, to allow for rapid filling. It is possible that an even simpler seal could be made at the factory by pinching the ends of the (hot)

extrusion at the same time that it is cut to length.

© **Manifold attachment:** Figure 5 shows the design for a prototype manifold to guide the fibers from the end of a module to a bulk optical connector. The final design would actually be of the “side-out” type used for some MINOS manifolds, but the figure demonstrates some of the considerations going into the design - the “side-out” manifolds are shaped so that the liquid level always remains below the optical connector. The manifold consists of two parts: the first is a guide for the fibers, and the second is a cover that excludes light from the manifold. The fiber guides occupy a minimal amount of space, so that the bulk of the manifold volume is available to accommodate possible expansion of the liquid scintillator in the event that its temperature rises significantly. An important feature of the manifold is the two fill-holes that are used for filling the detector after installation. They may also be used to remove the liquid scintillator if this becomes necessary. These manifolds would be manufactured either by roto-molding, which can be used to make pieces this size, or by injection molding, in which case separate, smaller parts would have to be joined.

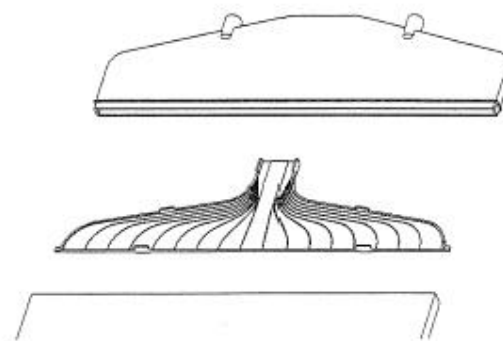


Figure 19 Manifold to lead fibers from the ends of scintillator cells to an optical connector.

Installation. Modules would be assembled and pre-tested at sites remote from the detector site. After shipping they would be

incorporated into the absorber panels in the same fashion as the solid scintillator modules. However, the PVC modules are much lighter and easier to handle, approximately 80 kg.

An important difference between the liquid and solid scintillator detectors is that the liquid scintillator would be added *after* installation. Scintillation fluors are supplied in concentrated form in 55-gallon drums, to be mixed in a large stainless steel vessel with mineral oil delivered by tanker-trailer. Mixed scintillator is pumped to the installed modules via permanent stainless steel plumbing lines containing quick-disconnects every 5 to 10 m. A flexible filling wand is used to transport the scintillator from these points to the fill-holes on the manifolds.

D6 Safety issues

PVC: We have a statement from the Health and Safety Administrator of the Division of Natural Resources, State of Minnesota, that there are no particular concerns with the use of PVC underground. He has an extensive background in mining and is familiar with both OSHA and MSHA regulations. This opinion has been echoed by safety experts at both Argonne and Fermilab. However, suitable precautions must obviously be taken to prevent an ignition source coming into contact with the modules. Pre-planning in case of fire is necessary.

Scintillator: The material safety data sheet for BC517L (Bicron, 1984) indicates a flash-point of 102°C and shows that none of the components (mineral oil, pseudocumene ~5%, small amounts of PPO) are particularly hazardous. Normal precautions with ignition sources should be taken, e.g., welding or cutting torches should never be used on or near a drum of scintillator, even when empty. Overexposure can cause irritation of the eyes

and excessive inhalation or swallowing of material can be dangerous. Precautions must be taken in the event of spills or leaks.

We have investigated the flammability of scintillator-filled extrusions. Test modules have been subjected to temperatures high enough to initiate burning of the PVC. Using a propane torch, it takes 0.75 to 1.0 minutes for a PVC extrusion to ignite. It self-extinguishes within 5 seconds when the torch is removed. Modules filled with scintillator are even more difficult to ignite, and also self-extinguish. The scintillator itself does not ignite easily and is self-extinguishing.

Of course, the fact that the cells are almost completely buried between planes of oriented strand board is a deterrent to spreading fire.

D7 Repair

In the history of large detectors, occasionally there have been disasters where an entire detector or a large part of it needed to be repaired or replaced; sometimes this has been due to a mechanical accident, sometimes due to a lapse in quality assurance. Although we can imagine no such scenario for a liquid scintillator detector, it is true that it is the only design for which large sections of the detector could be repaired or replaced *in situ*. For example, leaks occurring at the ends of the detector can be repaired. These are the only parts of the detector exposed to mechanical accidents. We have shown that the application of primer and glue is quite sufficient to repair small leaks, even with scintillator present. And, if something unforeseen happened to the liquid or the fiber, they could be removed and replaced.

Section E. Photo-detector readout and electronics

The light from the fibers will be converted to electrical impulses using avalanche photodiodes. These have been developed by the CMS collaboration for the readout of the CMS lead tungstate calorimeter and stable, low-cost devices are available from the manufacturer, Hamamatsu. The University of Minnesota was one of the three institutes responsible for this development, the others being Northeastern University and the Paul Scherer Institute in Switzerland.

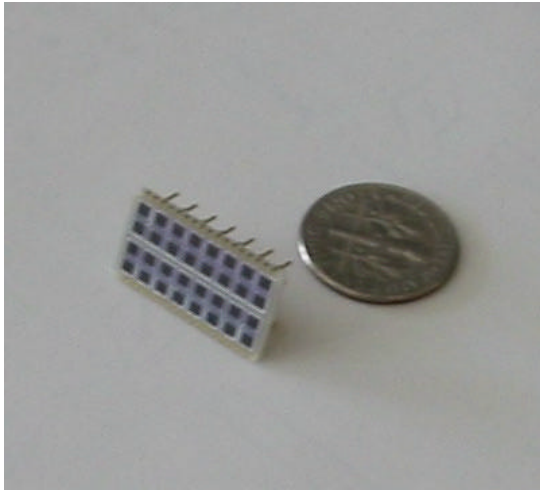


Figure 7. The new Hamamatsu APD array, shown with a dime.

An off-shoot of this development is a two-by-eight pixelated APD with a pixel size of $1.8 \times 1.8 \text{ mm}^2$. It has exactly the same junction structure and accordingly the same basic performance as the CMS APD. It is sold packaged in pairs to make a four-by-eight array. A photograph of the APD array is reproduced in Figure 7. We are proposing to use this device in bare die form, as it is the least expensive and simplifies the problem of coupling fibers directly to the photo-sensitive surface.

In this discussion we will start by describing the requirements of the photo-detector for the

Off-Axis detector, then, as APD's are relatively new devices to the field, the basics of their operation and the considerations necessary for their use. As we are proposing to use an APD that is based on the CMS APD, we will discuss the experience obtained with that device as a preface to describing the pixelated APD that we are proposing to use here. Then we will present a description of the proposed electronic readout of the APD and a discussion of the expected signal-to-noise for different levels of signal input.

E.1 Photo-detector Requirements: The photo-detector for this detector must be able to detect efficiently a single ionizing particle traversing a scintillator strip at a distance of 14.4 m from the photo-detector. It should be large enough so that it can collect the light from both ends of a 0.8 mm diameter looped fiber on a single pixel.

The estimates and measurements of the optical signal from a single mip, discussed in earlier sections, demonstrate that the photon signal for a normally incident mip will be 32 photons. The quantum efficiency for an APD in the region of the spectrum where the light is emitted is 85% and thus the signal that can be expected is 28 photoelectrons. This signal must be distinguishable from the electronic noise with high efficiency.

E.2 Fundamentals of APD operation:

The general structure of an APD is shown in Figure 8. Light is absorbed in the collection region, photoelectrons are generated and under the influence of the applied electric field they propagate to the p - n junction. At the junction the electric field is sufficiently high that avalanche multiplication of the electrons occurs by impact ionization, resulting in a net gain in current.

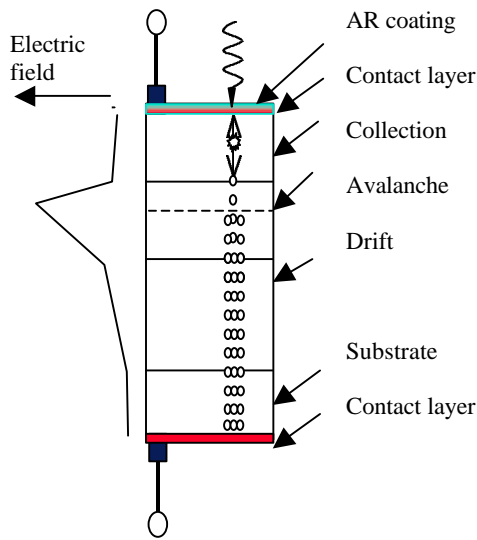


Figure 8. The basic structure of a blue/green sensitive APD. Light crosses the anti-reflection coating at the surface and is absorbed in the collection region. Photoelectrons drift in the electric field to the junction where they undergo avalanche multiplication.

The multiplication (M) of the current is determined by the electric field at the junction, and by the mean-free-path of electrons between ionizing collisions, which depends on both the accelerating field and on the temperature. The temperature dependence occurs because of the probability of electron-phonon scattering increases with temperature.

The amplification noise of the APD is limited by the fact that in the ionizing collisions of the avalanche process only a single secondary electron is emitted, as opposed to the 3 or more secondaries that are emitted at the first dynode of a PMT. This automatically limits the excess noise factor F (the ratio of the noise power output to the input noise power) to two or more, whereas for a PMT this is typically 1.6.

Other factors like non-uniformity across the diode's surface of the impurity gradients at the junction and other manufacturing imperfections lead to further increases in the noise performance of the diode.

In addition to this noise source, there is a contribution from electron-hole pairs generated thermally in the collection region of the diode. These electrons pass through the junction and produce a signal that is indistinguishable from the signal from a photoelectron. The thermally generated current is called the bulk current (I_B). The current of thermally generated electrons that do not pass through the junction is called the surface current (I_S). The contribution to the noise from I_S is suppressed by the gain and can be ignored for the Hamamatsu devices operating at gains in excess of 25.

E.3 APD Operation: The gain of an APD is dependent on the applied bias and the operating temperature. The normalized dependence of the gain, $\frac{1}{M} \frac{dM}{dV}$, for APD's

with this junction structure rises linearly with M and is equal to 3.7%/V at $M = 50$ and increases to 4.7%/V at $M = 100$. This voltage dependence is temperature independent. There is, however, a temperature dependence of the gain, $\frac{1}{M} \frac{dM}{dT}$, which decreases linearly

with temperature. When operated at $M = 50$, the normalized dependence is $-2.2\%/^{\circ}\text{C}$, while at $M = 100$ it increases to $-3.0\%/^{\circ}\text{C}$. This means that as the operating gain increases, the requirements on stability of the bias voltage and the temperature also increase.

One significant difference between APD's and PMTs is that once the bias voltage and the operating temperature are known, the gain can be predicted to within the accuracy of the temperature and bias measurements.

In this detector, we will maintain the operating bias to a precision of at least 0.2 Volts and control the temperature to 0.5 °C.

The choice of operating temperature for low-noise applications is determined by the need to suppress the bulk-dark current I_B . This is governed by an Arrhenius dependence. Roughly, there is a decrease in I_B of a factor two for every 7 °C that the temperature drops. Values for I_B of 4.5 pA/mm² of sensitive area are typical for the CMS APD's.

E.4 Experience with the CMS APD: The CMS experiment will use 124,000 APD's to read out the lead-tungstate calorimeter. Hamamatsu is the manufacturer of these APD's and it is expected that delivery of the whole quantity will be complete by the end of 2003.

In all, 124,000 APD's will be used by the CMS experiment and to date nearly 110,000 have been received from the manufacturer and 100,000 have been tested. The quantum efficiency for these devices is consistently at 85% at 550 nm as can be seen in the Figure 9

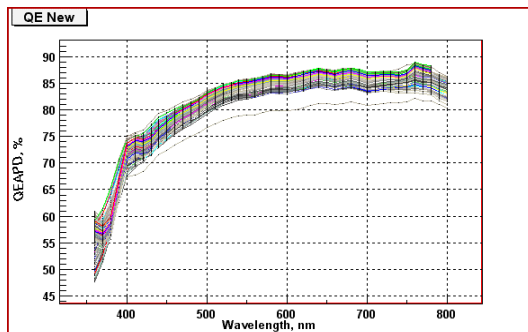


Figure 9 Quantum efficiency of several hundred APDs

The bulk current for an APD is obtained by dividing the dark current by the gain. A

typical plot for a CMS APD is shown in figure 10.

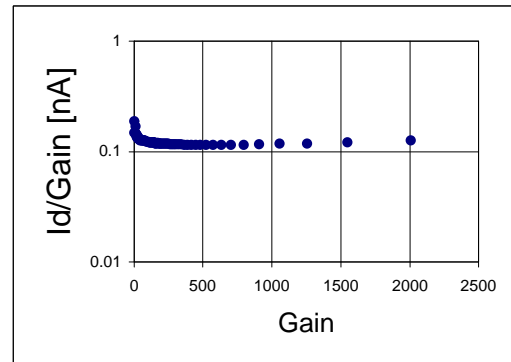


Figure 10. Dark current I_d divided by gain vs gain in a typical CMS APD. The asymptotic value of the current is I_B . These measurements were taken at 25 °C and yield a value of 116 pA or 4.6 pA/mm²

The excess noise factor F is governed by an approximate relation, that becomes more exact with higher gains, $F = kM + 2$, where k is a constant of the junction. A plot of F versus gain is shown in figure 11. At an operating gain of 100 the excess noise factor is 2.5.

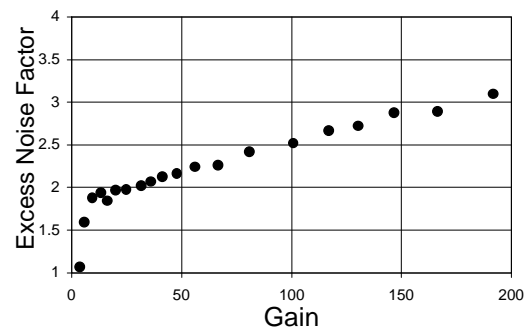


Figure 11. Excess noise factor, F , for the CMS APD.

E.5 The APD for this Detector: Samples from the manufacturer of the array that we are planning on using has been studied at Minnesota and Fermilab. The manufacturers specifications are given in table 1.

Table 3 APD specifications for Off_Axis Detector

Pixel Size	$1.6 \times 1.6 \text{ mm}^2$
------------	-------------------------------

Pixel pitch.	2.3 mm
Pixel Capacitance	10 pF
Bulk Dark Current (I_B)	10 pA.
Peak Sensitivity (λ)	600 nm
Operating voltage	400 ± 50 V

We have measured the pixel gain and pixel separation for one of the sample arrays. Our results are shown below in Figures 12 and 13.

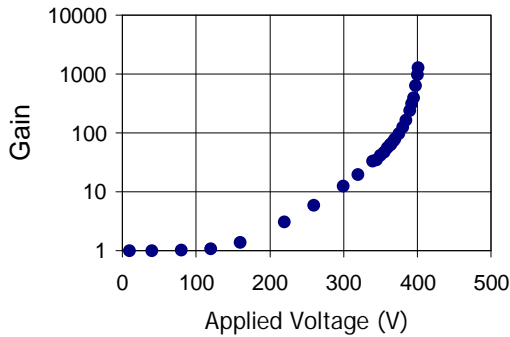


Figure 12 Gain vs applied voltage

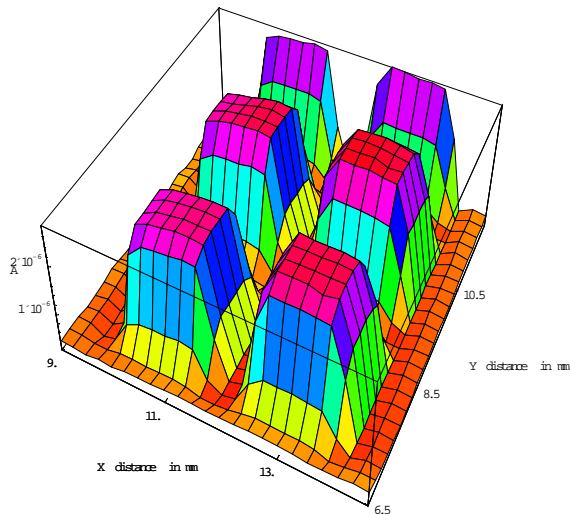


Figure 13. Fine point scan across part of the APD array

E.6 Electronic Readout:

For readout of these APD's we will need a low-noise preamplifier that can sample the signal throughout the 10 μ sec spill. The architecture we are considering is based on the Fermilab MASDA chip and the SVX4. The signal is amplified with a high gain integrating amplifier with an RC time constant of ~ 350 nsec and whose output is strobed into a switched capacitor array every 500 nsec. At the end of beam spill the signals in each capacitor are connected via an analog multiplexor to a 40 MHz 10-bit ADC, with one ADC for each 32 APD channels. Trigger primitives are constructed locally, sent to the trigger processor and, in the event of an interesting event, the whole of the event data is readout.

Noise: With the MASDA chip a noise level of ~ 350 electrons has been achieved without matching of the input capacitance with that of an APD pixel. Thus this figure should be seen as an upper limit achievable with a practical mass-produced device. We will run the APD at a gain of 100, which reduces the effective equivalent noise charge (ENC) to 3.5 electrons at the photo-detector input.

For two arrays of 16 APD pixels we have measured the average bulk dark current (I_B) per pixel to be 10 pA. This is consistent with the bulk dark current of the CMS APD: 5 pA/mm², corresponding to a 12 pA/pixel. A current of 10 pA corresponds to a current of 10 electrons every microsecond. By lowering the operating temperature by 43°C to -18°C (0°F) we will reduce the current by a factor of 64 to give a background rate of ~ 1 thermally generated electron per microsecond.

The requirements for the readout are then to detect a signal with an average value of 37 photoelectrons spread out over an interval of ~120 nsec (this interval is determined by the differences in arrival times of the scintillation light from the two paths along the WLS fiber), with a background rate of 1 thermally generated electron per microsecond with an amplifier with an effective ENC of 3.5 electrons.

The response to exactly N electrons measured with an APD operating with gain M with an excess noise factor F read out with an amplifier with an ENC at the input is given by the expression:

$$P(x, N) = \frac{\exp\left\{\frac{-(x-N)^2}{2\left[F-1+\left(\frac{ENC}{M}\right)^2\right]}\right\}}{\sqrt{2p\left[F-1+\left(\frac{ENC}{M}\right)^2\right]}}$$

This expression then is convoluted with a Poisson distribution to give the estimated signal shown in Figure 14.

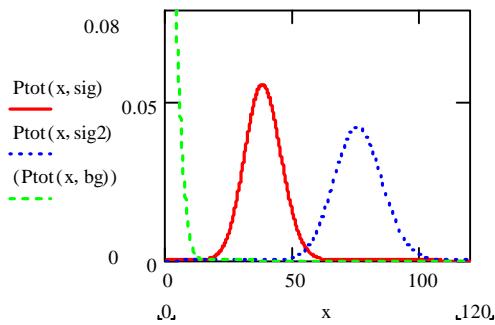


Figure 14. Signals from noise, 1 mip, 2 mip.

In this plot the signal distribution for the thermally generated background, a single normally incident muon and for two normally incident muons is shown. It can be clearly seen that there can be good

discrimination between, one, two and no normally incident muons crossing the far end of the scintillator strip.

Proposed Architecture: The architecture that we are considering is based on the SVX-4 structure. This consists of an integrating preamplifier, one per APD pixel, whose output is coupled to a switched capacitor array (SCA). For this application an array of 20 capacitors is sufficient. During the 10 μs spill the output of the amplifier is stored on the capacitors in the SCA at 500 ns intervals. The integration time for the preamplifier will be ~350 nsec.

After the beam spill, the signal on pairs of capacitors corresponding to intervals of 1 μsec will be compared one by one. That is, if the capacitors are labeled C_1, C_2, C_3 etc. then the charge on C_3 is compared with that on C_1 and the difference coupled through an analogue multiplexer to an external 10-bit ADC where it is digitized and stored. When the conversion is complete the charge on C_4 and C_2 will be digitized and stored. When all the voltage differences for that pixel have been digitized the process will be repeated for the SCA associated with the next pixel. A single 40 MHz ADC will be able to digitize the signals from the 30 pixels that are used to readout a module in 15 μsec.

Once the conversion is complete trigger primitives can be formed and sent to a trigger processor, which will collect all the primitives from the detector and select events to be readout for further processing.

The organization of the readout will be into pairs of modules with the complete front-end readout of two modules in a single readout box. We will use two 16-channel APD arrays to readout the 30 strips of a single module, thus four APD arrays per box. The readout box will be located where the two modules

join. The mechanics of this will be discussed in the next section. Here we discuss the electronic architecture.

The 4 voltages to bias the four APD arrays (400 ± 50 V) will be supplied from on-board Cockroft-Walton voltage generators. (These are currently under design by the Fermilab electronics group.) Each module will have a 30 channel SCA chip readout with a single 40 MHz 10-bit ADC. The output of the two ADC's in the readout box will be stored in a FPGA or a custom ASIC, which will also generate the trigger primitives and store data until a trigger accept is received. The APD's will be cooled with single-stage Peltier coolers and, to prevent condensation, the readout box will be filled with dry nitrogen. The thermal power generated in the four APD arrays is $64 \times 400 \times 10^{-9}$ W, or 10 μ W, the most significant thermal load will be from local conduction along the fibers and through the electrical interconnects.

Temperature monitoring and control, clock regeneration and IO functions will be controlled with a low-power I2C circuit. In the design of the readout box the APD's will be mounted on the opposite side of the board from the other electronic components to minimize the thermal load.

Connection between the readout boxes and the data acquisition will be performed using a standard readout protocol such as 1 Gbit Ethernet or Firewire, whichever is the most economical.

E.6 APD Housing

A box housing the APDs and their associated electronics will be connected to the end of this scintillator manifold. The manifolds are designed such that two scintillator modules can connect into a single APD box. This is achieved by flipping over one module by 180

degree. Only one type of manifold has to be produced. (See Figure 15)

The fibers enter the optical connector in a pattern that is compatible with the spacing of the sensitive areas of the APD array. The two fibers from a single scintillator strip will be routed as closely as possible to each other. They will be placed on the diagonal of a single 1.8×1.8 mm² APD pixel. The optical connector is matched to two 2×8 APD pixel arrays. The connector is not rigidly connected to the manifold, but can be shifted and twisted by about ± 2 mm. This is achieved by having gimbals at the connector. (See Figure 16 for details.) This construction ensures that a moderate misalignment of the two 14.4-m long scintillator modules can be accommodated, and does not compromise the light seal at the APD box.

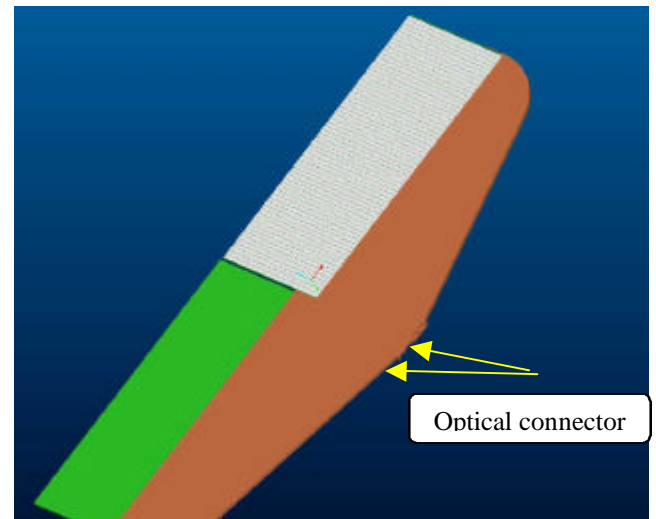


Figure 15: The end of two scintillator modules. 32 strips are grouped together. All fibers from one module are routed within a manifold to an optical connector. The two manifolds for the left (green) and the right (white) module are identical, but flipped by 180 degree. The fibers of two scintillator modules are routed into a single APD box, which will be plugged onto the optical connectors.

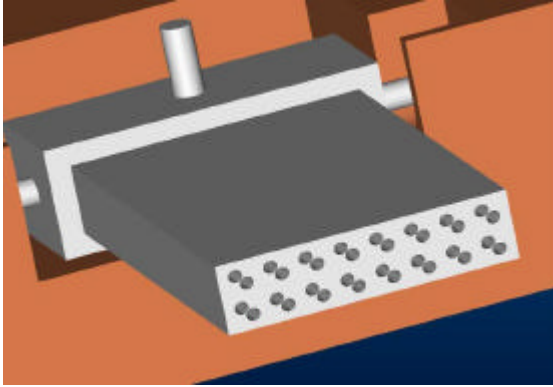


Figure 16: Optical connector for fibers from 16 scintillator strips. The relative spacing of the fibers is such that the two 0.8 mm fibers from a single strip are routed to a single APD pixel. APD pixels are arranged in a 2x8 array. Gimbals hold the connector in position allowing for some limited movement.

The APD housing has to fulfill several functions:

1. Match fibers to APD arrays
2. Light tight connection to scintillator module
3. House APD and electronics
4. Remove heat from electronics and Peltier cooled APDs (-20 degree C).
5. Structural strength

The design sketched in Figures 17 and 18 achieves this: The APD will be bump-bonded onto a printed circuit board (PCB). There will be an injection-molded collar around the APD arrays to receive the optical connector of the scintillator modules. This collar is located to 100 micron precision with respect to the APD array and will define the positioning of the fibers with respect to the array. The PCB will have a cutout behind the APD array to allow a thermoelectric cooling element to be placed in thermal contact with the array. The hot side of the Peltier-element will be attached to a passive heat sink. The other electronics components, especially the DC/DC converter, will also be connected to the same heat sink.

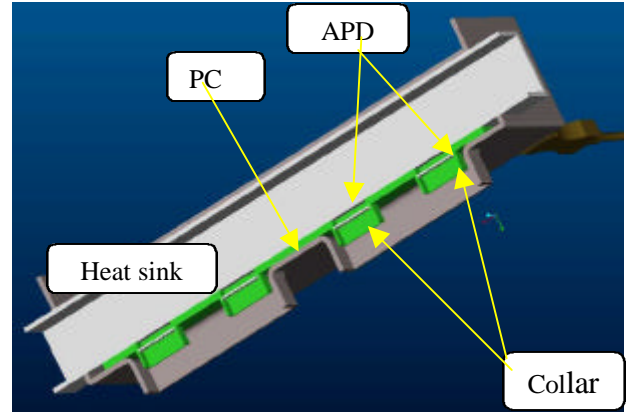


Figure 17: Cutout of the APD box. This APD box will receive the signals from two scintillator modules. Their optical connectors will plug into the collars (green), which locate them in respect to the APDs. Peltier-elements (not shown) will sit behind the APDs in a cutout of the PCB and will be in thermal contact with the heat sink.

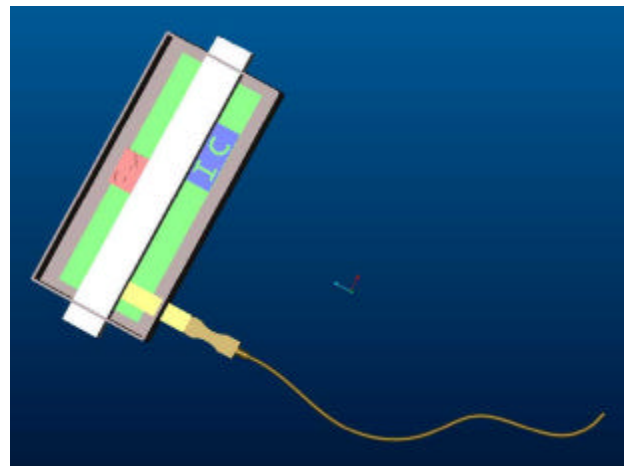


Figure 18: Conceptual top view of APD box. The optical connectors and the APD arrays are below the PCB (green). The electronics (IC, blue) and the HV generator (CW, red) are thermally coupled to the heat sink (white).

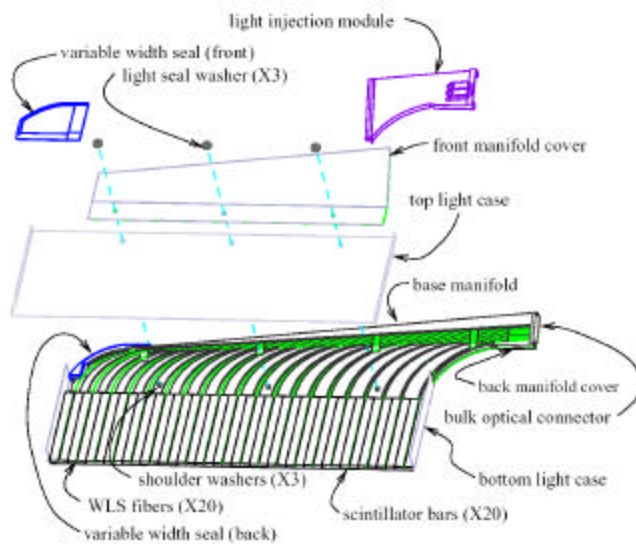
The APD arrays, the PCB, the heat sink, and the electronics will be surrounded by an injection-molded box. This plastic box is inexpensive but will not act as a Faraday cage. Methods to imbed a metal grid or use conductive plastic are currently being investigated. The box will also contain connectors to supply the electronics with low voltage, clock signals and electronics

readout. Any type of connection is relatively easy to implement in this box. However, care must be taken to make the box serviceable and light tight.

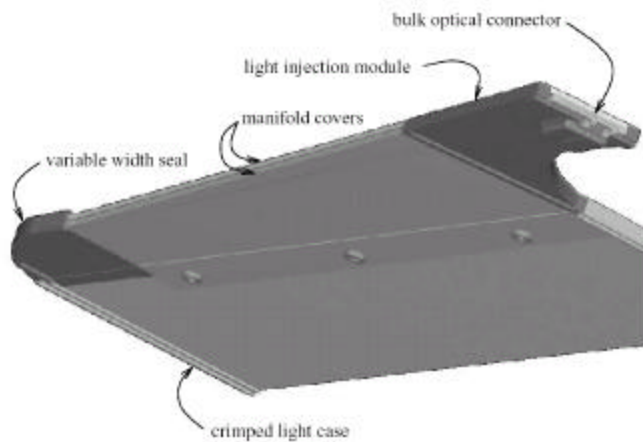
Section F. Solid scintillator module design

The solid scintillator module engineering will be a direct derivative of the design successfully utilized in the MINOS detector. The liquid scintillator alternative is described in a separate section. The modules are constructed at remote sites and installed rapidly at the detector site.

Modules of the off-axis detector share the overall structure of the MINOS modules. A module consists of groups of scintillator extrusions wrapped in metallic light-tight cases. The light case provides structural integrity and fireproofing as well as a light seal. WLS fibers are guided out of the modules by way of manifolds at their ends.



(a) Exploded view.



(b) Assembled view.

Figure 20 A "perpendicular side-out" manifold assembly from the MINOS detector, including the

The manifold architecture of the off-axis detector is similar to the “perpendicular straight out” manifolds utilized in the MINOS detector. This MINOS manifold style is illustrated in Fig 1. A “base manifold” comprises the core of the manifold system. It contains grooves, which precisely control the position and bend radius of each optic fiber. Front and back covers light seal the manifold assembly. A “light injection module” enables illuminating fibers for calibration and operational verification.

The MINOS manifolds used “variable width seals” to enable matching the width of each module to the extrusions contained within it. In contrast, the off-axis modules will be of fixed width, eliminating the need for these parts.

The MINOS modules have a bulk optical connector installed at the tip of the manifold, as shown in Fig b. The off-axis modules will replace the bulk optical connectors with light sensors; the light-to-electronic signal conversion is performed directly at the modules eliminating the need for clear fiber harnesses.

The MINOS modules utilize double-ended readout, so manifolds are attached to both ends of all far detector modules. The off-axis modules will utilize single-ended readout.

MINOS scintillator extrusions contain a single groove for WLS fibers. A single fiber protrudes off of both ends of each extrusion. The protruding fiber ends are routed through the manifolds at each end to the bulk optical connectors.

In contrast, the off-axis detector extrusions will contain two grooves.

A circular groove will be cut at the bottom of each extrusion during manifold construction. This circular groove will connect the two extruded grooves. A single, continuous fiber will then be threaded through both grooves in a “U”-shaped path. Therefore, two fiber ends will protrude from the top end of the extrusions, while no fiber protrudes from the bottom end. Both free fiber ends will be threaded through the manifold to the light sensor installed at the manifold tip.

The MINOS far detector requires three separate manifold styles. All were subject to demanding height constraints to meet the dimensional specifications of the Soudan mine cavern and access elevator. The off-axis detector will utilize only one manifold style on all modules. The height constraints are relaxed. These changes will enable simplifying the light sealing procedure at assembly.

The similarity of the off-axis modules to the MINOS modules reduces the engineering effort and risk required for their design. Nevertheless, engineering design and optimization effort is needed to address the differences between them. The additional engineering investment will result in system benefits of lower cost and higher performance.

Specifically, the module-engineering program will address the following changes:

- All optic fibers in the MINOS manifolds are in a single plane. The off-axis manifold system requires organizing the fibers into two planes to match the geometry of the optical sensors.

- The bulk optical connector attachment must be re-designed to support the light sensors.

The highest cost component of the MINOS module is the base manifold. They were fabricated by machining grooves into plates of foamed PVC. The cost was driven by the machining time.

The optic fibers follow a straight-line path at the back of the bulk optical connector. They then transition to an arc to change direction to match the orientation of the scintillator extrusions (see Fig b). Most of the machining time for the base manifolds was invested in cutting the flared arcs above the scintillator extrusions.

Controlling the fiber bend radii is critical to ensuring the long-term integrity of the detector. Providing individual fiber grooves helps guarantee an acceptable bend radius, as well as facilitating assembly. However, the fibers do not actually touch the walls of the arced portion of the manifold grooves; their bend radii are controlled by contacting a wall at the top of the straight-line portion of the fiber grooves.

Eliminating the base manifold arcs will reduce the cost of the off-axis manifolds. The fiber grooves will only define the straight-line portion of the fiber path. The portion of the base manifold between the scintillator extrusions and the grooves will be simplified to a flat plate that extends only as high as the bottom of the fiber groove.

Engineering costing will determine whether the lowest cost manifold can be obtained by machining the fiber grooves in foamed PVC or assembling the grooved portion of the manifold from a series of injection molded sub-components. The size of the grooved portion of the manifold is likely to exceed

the capacity of an injection-molding machine. Therefore, the grooved portion will likely need to be assembled from two or more injection molded pieces.

- The feasibility of lowering the cost of the light case by changing the material from aluminum to steel will be explored.
- The fiber groove paths will be re-optimized to improve the light seal within the context of relaxed manifold height constraints.
- The design of the manifold covers will be re-visited to further improve their light sealing capability, particularly in the context of eliminating the variable width seal.

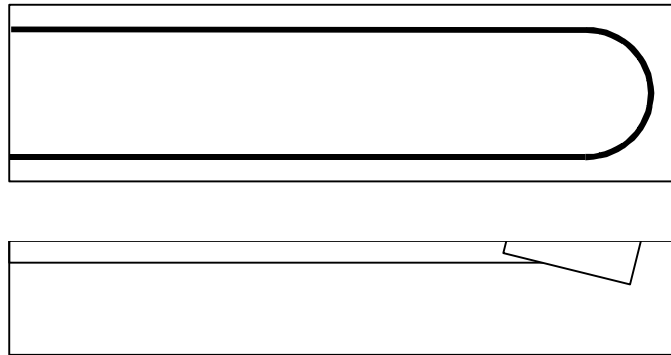
F.1 Module fabrication

The basis of fabricating the off-axis scintillator modules is the MINOS assembly techniques. Similarly, the MINOS equipment as a starting point closely models the equipment needed for the off-axis detector. There are, however, differences in the proposed off-axis detector modules that warrant improvements from the MINOS model. Additionally, the quantity of modules to be produced is greatly increased requiring greater efficiencies. The equipment needed is described below. The most basic differences are in geometry and quantity. The off-axis modules are 1.8 times longer than MINOS modules, have single ended dual fiber readout, and come in one geometrical flavor.

Cutting Station: All of the modules are rectangular in shape and are of the same size. The individual scintillator strips are therefore equal in length. Additionally, there is a lower requirement for assembly tolerance which translates into a reduced

tolerance requirement for the scintillator. The scintillator length tolerance is assumed to be $\pm 5\text{mm}$ and is believed to be a tolerance that can be produced at the extruder eliminating this step from the factories. The cost of a simple MINOS style cutting station is included as a contingency in the event the cut quality from the extruder is deemed unacceptable.

Scintillator fiber groove cutter: A simple tool and fixturing is required to produce a loop groove at the end of the scintillator to hold the fiber loop. This is currently imagined to be as simple as a hole saw and drill fixtured on an angle to cut the loop. Some minimal effort should be used to design and test this concept to verify the quality of cut. The hole saws will be a replacement item.



Assembly Trays: Assembly trays provide an assembly surface, fixturing, a safe method of transport, and hold the modules during curing. The modules are assembled and remain on these trays moving between assembly stations until the final stage of assembly. The trays are very similar to the style used in MINOS. The trays are approximately 15m in length to hold the 14m modules. The tray material will be a sandwich panel construction of aluminum skinned over an aluminum honeycomb core for optimized stiffness vs. weight. The trays are nominally 1" in depth. This dimension will be investigated with respect to its coupling to curing rack components and iterated to optimize both designs.

Light Case Forming Machine: The light cases for the MINOS modules were fabricated through a series of manual operations. The light case began as a flat strip of 0.5 mm thick aluminum. The material was slit to width using a custom

built rolling shear, which was pulled along the length of the light case. Vertical flanges (see Fig. 6(a)) were then formed using a “tinner’s tool”. Slitting the light cases to width at the MINOS factories was necessary to enable varying the width of modules. Since the off-axis detector modules are of fixed width, the light case material will be pre-slit to width by the material vendor. The efficiency gained will lower manufacturing costs and times.

Further efficiency will be gained by designing semi-automatic machines to form the vertical flanges on the light cases. The forming machines will be based on roll forming methodologies successfully developed for the MINOS crimping machines (see Fig. 7). The machines will facilitate the handling of the longer 14.4 m modules, as well as reducing fabrication times. The quality of the flange will improve as well.

Light Case Crimping Machine: The light-case crimping machine is designed to create a mechanical light seal on both 14.4 m edges of the module light case. The crimping machine will be directly based on the successful design developed for the MINOS modules. A brief description of the MINOS machine is provided here.

Engineering changes required to adapt this design to the off-axis modules are then described. The top and bottom of the light case are each designed with a vertical flange that is formed by the case-forming machine. The vertical flanges of the top light case are nested within the vertical flanges of the bottom light case (see Fig. 6(a)). The crimping machine re-shapes these flanges into a light tight seal in one pass (see Fig. 6(b)).

The crimping machine consists of a table, a truck that traverses the length of the table on

linear guides, and a 10-station rolling head (see Fig. 7). The head can be rotated from one edge of the module to the other within the truck, so both edges of the module can be crimped without rotating the module. The crimper is hand cranked to minimize safety concerns. It is capable of crimping an 8 m edge in 50 seconds.

The MINOS modules utilized 0.5 mm thick aluminum light cases. If the same light cases are used in the off-axis modules, the MINOS crimper heads may be re-usable. The table and truck will need to be rebuilt to accommodate the increased length and width of the off-axis modules. Steel light cases are also under consideration for the off-axis modules in an effort to reduce their cost. Utilization of steel will require engineering modifications to the crimping heads. In particular, unhardened rolls were utilized for MINOS; these would have to be replaced with hardened rolls.

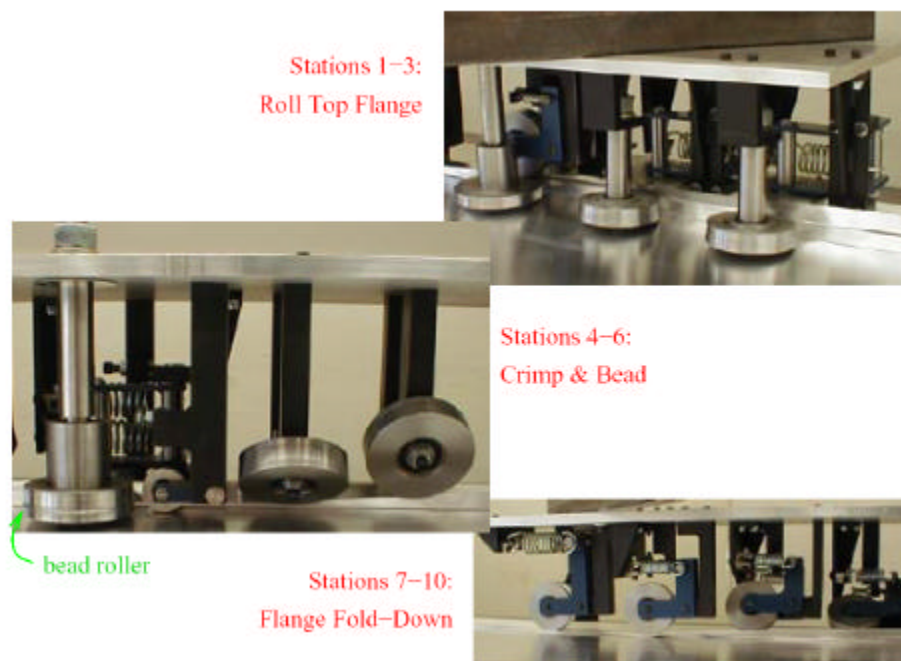


Figure 0.21 Stations of the light case crimping machine rolling heads.

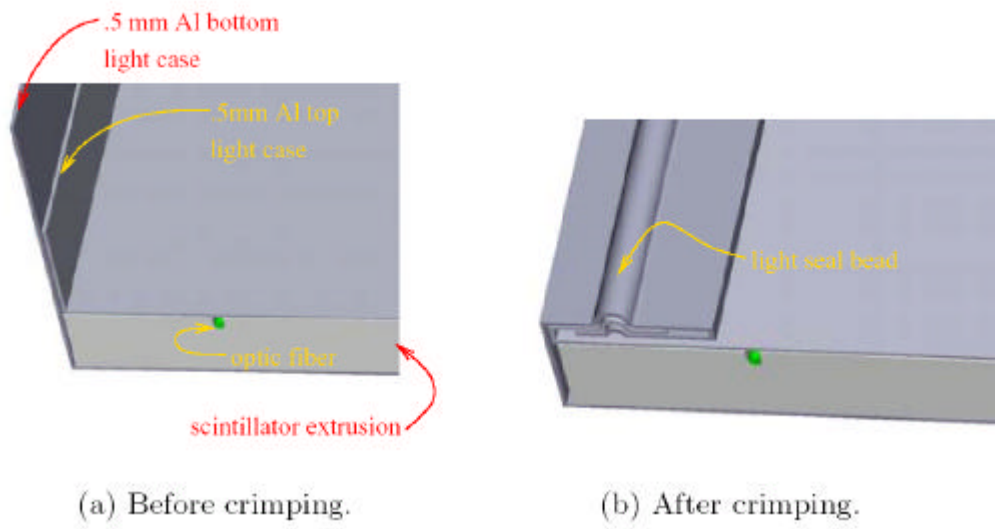


Figure 0.22 Edge of light case before and after crimping.

Module Assembly Tables: The module assembly tables are lightweight structures that after accepting the assembly trays serve as the assembly station. In MINOS, these tables had ball transfer rollers on the surface to allow easy transfer between the tables, work stations, and storage racks. Due to the stiffness of the assembly trays and low contact area of the ball transfer elements, high contact stresses occurred when only the few balls supported the load. Engineering effort will be needed to design a similarly economical and efficient transfer mechanism that provides more contact area and compliance to reduce the contact stress that lead to tray damage in the MINOS trays.

The tables will have castors mounted allowing easy movement between stations. These tables might additionally feature an elevation mechanism to be able to access storage racks with additional shelves as compared to MINOS.

Reusable Vacuum Seal: In the MINOS assembly disposable sheets of polyethylene were used for vacuum sealing of the modules during the adhesive curing in the bottom and top assembly steps. The polyethylene was sealed to the table using disposable vacuum sealant tape. For each module assembled, this operation was done twice. With the increase in module size and quantity, this translates into a 10x increase in these disposable items. Additionally, the installation of the vacuum tape was time consuming. To save these costs and waste as well as reduce the time at the assembly step, a reusable vacuum sealing fixture should be developed. Engineering effort is required to formulate the details of a practical design.

An initial design for such a system is made using a foldable "piece-wise rigid" frame that has the sealing material (polyethylene film for example)

already connected in a sealed fashion. For reusability, this sealing material would be a dual material construction using lightweight polyethylene for the air seal with an interior member (in contact with the modules) of a tear resistant fabric such as Tyvek to provide long life to the sealing material. The plastic would be of area approximately 4 x 48 feet matching the outline of the assembly tray. The foldable frame when assembled would form the rigid gasket interface that would be clamped to the perimeter of the table. The frame pieces would be made to optimize stiffness versus weight for ease of handling and to reduce clamps needed. The individual pieces might be on the order of 4' lengths with ends made to quickly inter connect allowing for quick assembly / disassembly over the assembly tray. Simple clamps would then be attached to make the firm seal. The clamps needed would be on the order of 30 per tray under vacuum at any time at each factory and might require some customization to fit into the tight clearance of the curing rack shelves. These vacuum seals would be needed in the quantity of between 8-16 per factory depending on the factory model and the adhesive curing times.

Automated glue dispensing: In MINOS, the glue for laminating the top and bottom skins was applied and spread by hand. With the increased production rate demands and module quantity, an automated commercial glue application system should be investigated. This will speed production and more consistently place glue allowing more efficient use of the expensive structural epoxies.

Module Curing racks: The module assembly trays are stored in indexing curing racks between assembly stages for epoxy curing as well as production buffering purposes. Unlike the MINOS rack design, the racks in this case will not be designed to be portable due to the greater length.

Additionally, an effort will be made to increase the number of shelves to 8 or higher as this will play a role in the factory model where 8 modules are built per day. Due to shelf structural parts and the formed bottom lightcase, there are physical limitations to the number of shelves that can be made to accommodate a fixed height assembly table.

Similar to the ball transfer roller problem described for the assembly tables, the rack shelves need a similar solution that properly distributes the tray loads and reduces the contact stresses.

In addition to the length increase, as part of the redesign from the MINOS racks, an optimization needs to occur between the number of support points, the shelf structure, and the table heights to maximize each rack storage capacity. As mentioned when describing the assembly tables, adjustable height assembly tables could solve this. The cost of additional racks versus this solution would need further investigation.

Fiber Gluing Machine: The fiber gluing machine is based fundamentally on the MINOS machine where an assembled module bottom is placed on a table and a carriage contained the fiber, epoxy, and Mylar tape is automatically driven over it applying glue. Using the MINOS machine as a starting point, redesign effort would be done to further automate the machine and increase the speed of production as well as improve the machine safety. The fundamental difference between the MINOS and off-axis gluing machine is the gluing a single looped fiber simultaneously into a dual grooved scintillator.

This dual fiber gluing would be accomplished using a fiber take-up roll placed on the carriage alongside the main

roll. The take-up roll would contain an amount of fiber equivalent to the length of the scintillator plus that needed to route to the optical connector in the manifold. The machine would then start at the non-manifold end of the scintillator and place fiber into both grooves simultaneously using the same techniques of MINOS where the glue is deposited automatically, fiber is placed into the groove through the help of a compliant pushstick, and Mylar tape is pressed down over the top. At the end of the cycle at the manifold end, the take-up fiber would be fully unwound, and the fiber from the main spool would be automatically cut and to a length allowing for routing to the optical connector. This automatic cutting would be part of a mechanism that would hold the fiber and then rethread it into the take-up reel so that during the return trip of the carriage to the starting point, the fiber would be automatically wound on the take-up reel ready for the next pass.

As an improvement to the MINOS machine, the gluing speed would be increased. This was not optimized in MINOS and there were clear indications that substantial speed increases could be made with no loss in quality. This effort necessitates additional safety devices due to the increased moving mass as well as more sophisticated controls of the motion and fiber tension.

Additional design improvements would be made to automatically capture the fiber at the starting point and engage the associated gluing components so to greatly reduce the operators contact with the fiber and the epoxies. This would leave the operator available for QC, fiber threading in the manifold, and recovering the machine from any operational faults. This can be accomplished with a simple mechanism at the end of the table, independent of the carriage.

The glue machine would continue to be controlled by a PLC as in MINOS. With the above mentioned improvements in control and automation, more sophisticated control hardware (more powerful PLC), sensors, and power transmission components will be needed.

These features would add development and component cost to the machine but these would be easily offset by the production gains.

Effort will also go into researching a commercially available epoxy dispensing system that is more compatible with the optical epoxy chosen and has easier maintainability and reliability.

Module Mapper: The mapper is a fully automated servo driven X-Y scanning coupled to a data acquisition system. The mechanical portion of the mapper will follow closely to the MINOS style with the trivial increase in length to accommodate the longer modules. Some minor redesign of the mechanical drive and motion control components may be made to customize the mapping application to the new modules.

F.2 Factory labor and production

The 4000 modules for the MINOS Far Detector were produced in two factories, at Caltech and Minnesota (Argonne produced the Near Detector Modules). These factories were initially designed to produce 18 modules per week with 7 FTE plus a supervisor. They were equipped with space to permit up to one additional epoxy cure overnight. Production was limited by the number of curing racks in the factories and

could have been designed for increased throughput. These factories operated for roughly three years and were staffed for one shift per day.

The factories operated at full production within 10 weeks of the start of production and eventually exceeded the production goals in both throughput and efficiency. The Minnesota factory, averaged over the entire production, required 16.5 hours of labor per MINOS module with a weekly production rate of 19.7 modules per with 7.0 FTE.

The production method we propose for the Off-Axis modules is a refinement of the techniques used in MINOS. Areas that were most labor intensive were either eliminated in this design or machines are envisioned that will improve productivity. Despite the fact that the Off-Axis modules are larger, our analysis shows that we will be able to achieve a steady-state production rate of 20 modules per week with the same manpower. The production needs of the experiment can be met using three factories, each running two shifts over the course of 3.5 years after the completion of outfitting, including a 10 week learning curve to achieve high quantity, high quality steady state production. We anticipate the initiation of production in parallel with the civil construction at the detector.

Section G. Absorber Structure Construction

The standard unit of absorber to be used in construction is an eight layer laminate 8'x48', made of oriented strand board (OSB), which we will call a *stack*. Twelve stacks, each with a mass of about 5 tons, make up one detector plane. The stack will also serve as a container for two active detector modules, described elsewhere. There are several unique features of this laminate that

allow it to be built efficiently into a monolithic structure.

The stacks are placed side by side to form a *plane* of absorber and scintillator which are then arranged to provide alternating horizontal and vertical views. Adjacent units and successive planes are screwed to each other for lateral stability while the load of the structure is transferred to the floor through the OSB itself. A detector with 50 kT total mass contains 885 planes.

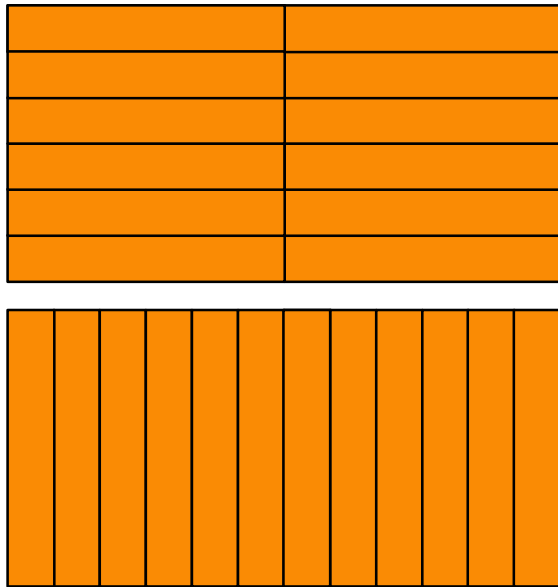


Figure 23 Layout of stacks showing arrangement of alternating layers. Each stack contains two scintillator modules.

Stack Composition

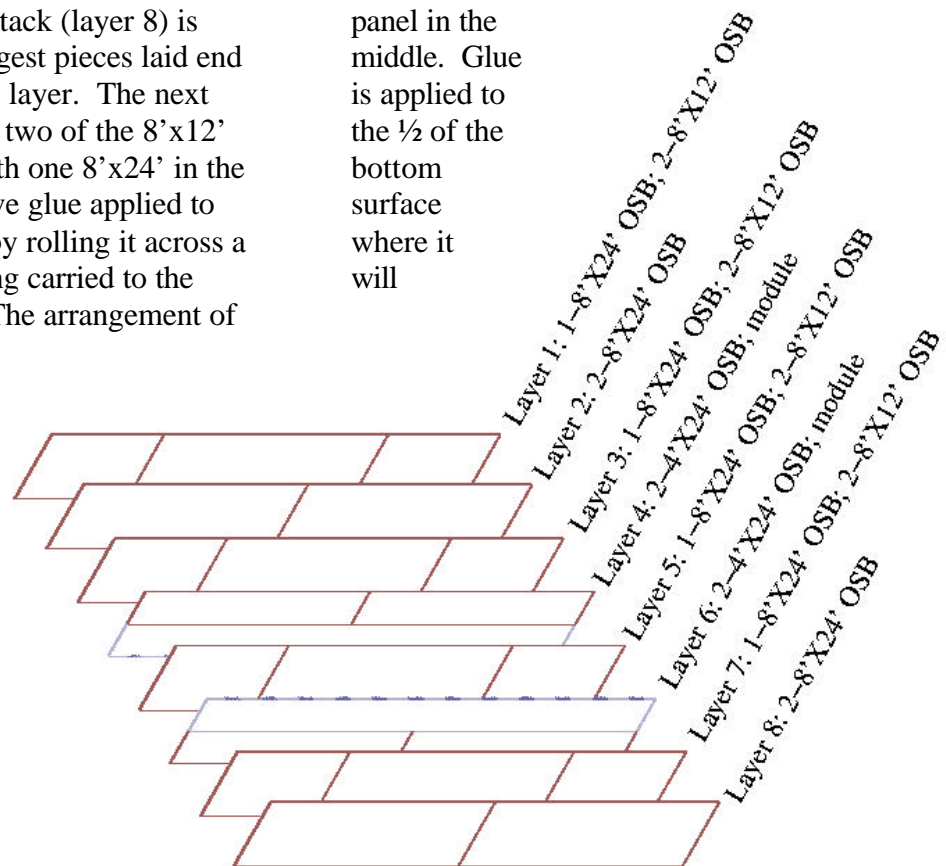
OSB is available from the manufacturer in any size up to 8'x24', limited by the size of the press with a thickness ranging up to 1.125". It is available in smaller sizes, most easily in 4' increments. The stack is comprised of 3 different sizes of 1" thick OSB, readily available from the

manufacturer: 8'x24', 8'x12', and 4'x24'. This makes the assembly of the stack most efficient by minimizing parts while emphasizing structural integrity. The design of the stack, detailed below, gives a strong and rigid laminate 8" thick.

The bottom layer of the stack (layer 8) is made from two of the largest pieces laid end to end to form the 8'x48' layer. The next layer (layer 7) is made of two of the 8'x12' pieces lain at the ends with one 8'x24' in the middle. These pieces have glue applied to the bottom of the board by rolling it across a glue roller while it is being carried to the stack assembly station. The arrangement of these pieces insures that there will be solid wood in the layer over the butt joints of the preceding layer, giving strength to the structure. This structure continues with the addition of each layer. The next layer (layer 6) is the first with an active detector element inserted.

The active detectors are 4' wide and 48' long, taking up only 1/2 of the layer. The other 1/2 consists of two 4' wide OSB panels, each 24' long, so that the joints will not be aligned. The next layer (layer 5) is the same as the second, two 8'x12' pieces at the ends, with one 8'x24'

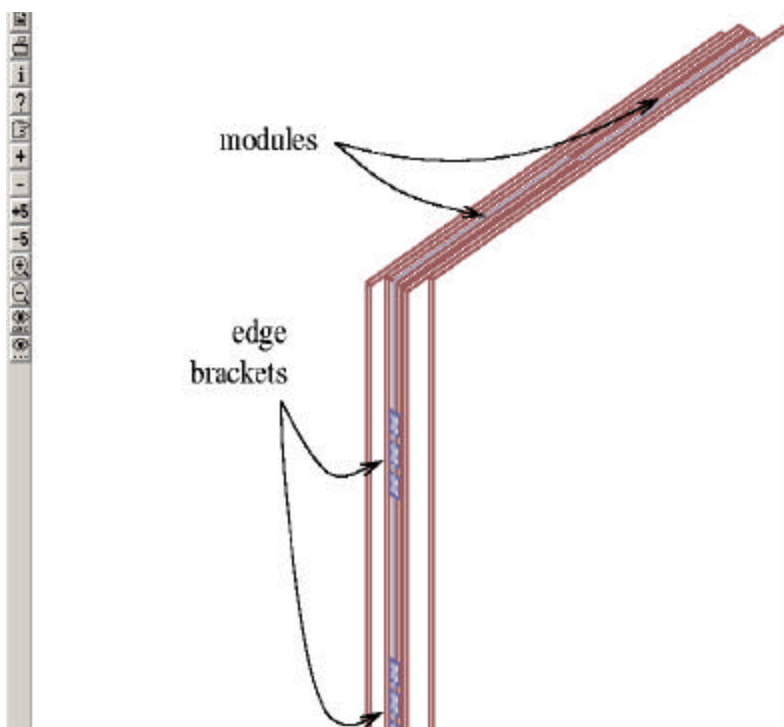
panel in the middle. Glue is applied to the 1/2 of the bottom surface where it will



contact the wood in the previous layer. The next layer is an active layer identical to layer 6 with the positions of the module and wood panels reversed. The next layer is identical to the layer 5, 8'x24' wood, with the glue on the bottom half to meet the wood in the sixth

layer. The final two layers are entirely wood panels as shown.

There are two more features built into the stack that allow it to be efficiently installed, and structurally stable. The first is an edge bracket. This bracket serves two purposes, it positively positions and holds the active detector module and it provides a



structural stability to the stack so that it will hold together when lifted. It also holds the stack halves in position so that they will not pivot about the fulcrum created by the gaps above the active detector modules. A design for this bracket is shown in the figure. The other feature is that the outer panels of wood are offset so that their long edges stick out from the stack by 6" in opposite directions. This gives the stack flanges that allow for easy installation without revealing the active modules, and exposing them to possible damage. These flanges can be seen in the figure, along with the edge brackets.

Stack Construction

Vacuum lifting fixtures are used to move all the panels from convenient storage areas. Since there are few components, 3 types of wood, 1 type of active detector, and the edge brackets, the workspace can be relatively compact to maximize efficiency. The workstation can be easily fitted with guide blocks that will provide reference stops to produce the profile of the stack with the

proper flanges and provide consistent production of the absorber stacks. This process will produce approximately 10,000 stacks, underlining the need for efficiency and reproducibility.

Mechanical Integrity

A preliminary evaluation has been made of this structural design by three engineers: Tom Chase (Minnesota), Vic Guarino (Argonne), and Bob Wands (Fermilab). The most recent study was of the structural strength of individual stacks using an ANSYS FEA model. The model of a stack is shown in figure 2. To understand the limits of the structure the strength of the units with point supports in a horizontal orientation was tested. The results indicate that an extreme case of supporting the units at only the far ends would lead to buckling. However, adding a single additional point in the center of the stack would lead to small enough deflections and stresses to be within the allowed limits for the materials.

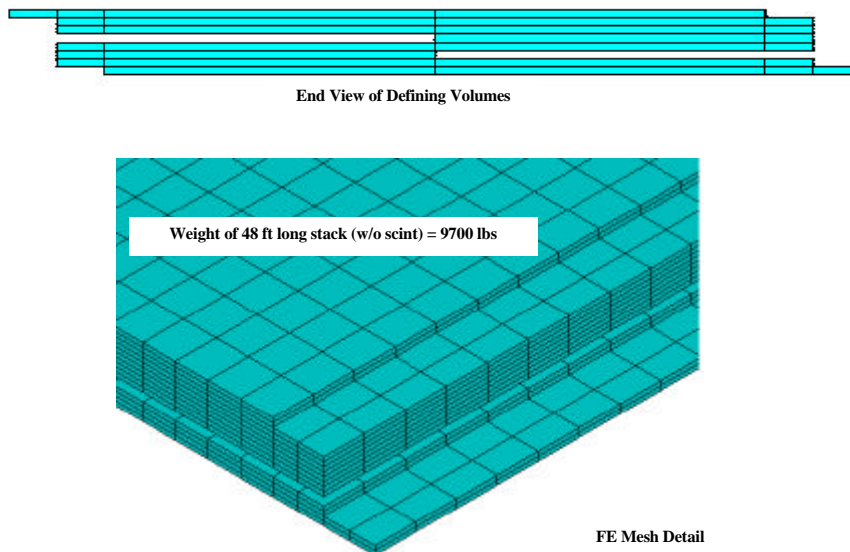


Figure 24. Stack layout and sample of the FEA mesh definition.

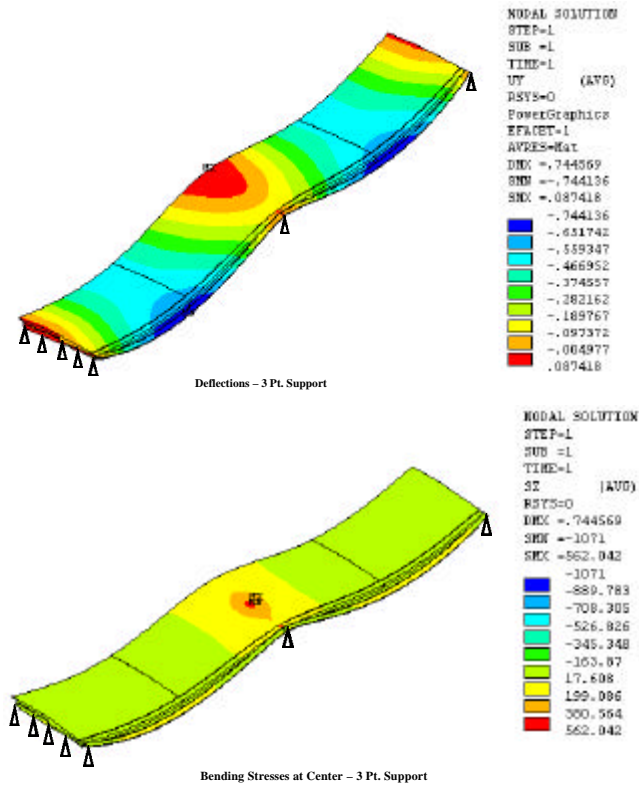


Figure 3. ANSYS calculation of deflections (top; maximum is 0.087 in) and stresses (bottom; maximum is 562 lbs) in a horizontal stack with only three support points under self loading.

Thus, due to the low pressures imposed (~15-20PSI) by self-loading, there are no buckling issues associated with the structural elements as long as the stacks are in an orientation close to vertical.

Using the techniques developed for MINOS Far Detector installation the stacks would be surveyed and shimmed every plane to eliminate significant horizontal forces other than those caused by expansion after installation.

The dimensional properties of OSB are well known to vary with both temperature, and more significantly, humidity. The primary structural requirements are to provide compliance in the monolithic structure to large variation in humidity. Like MINOS, the proposed Off-Axis structure will incorporate steel “bookends” to occasionally interrupt the monolithic structure. The bookends provide a vertical reference and anchor points. The verticality requirements in the Off-Axis detector are relaxed by more than an order of magnitude relative to those in MINOS.

Section H. Detector installation

Installation of the monolithic Off-Axis scintillator detector would follow the installation protocol of the MINOS far detector. The scintillator modules and readout components are produced at remote factories at Universities and Laboratories and shipped to the detector site. At the site the detector materials are received and staged, the modules are integrated with the absorber, installed into the detector, surveyed, and shimmed. Finally, they are mated with their photodetectors and commissioned incrementally.

The MINOS installation was a more technically challenging task in terms of the complexity of the operations and the duration of the single longest installation test (welding) and in terms of the mechanical specifications. Nevertheless, production had ramped to full efficiency by the eleventh week after beneficial occupancy of the detector hall. A similar ramp up is assumed for off-axis production. The near grade location of the detector leads to a significant reduction in staging problems and preassembly space, even though the volume of detector components is significantly larger than for MINOS.

The goal of this installation is to achieve a rate of one plane installed per shift or 8 planes per week corresponding to 12 detector stacks per shift. Including ramp up, the entire

installation process will take in 2.5 years to complete, proceeding in parallel with the tail end of the module fabrication process.

As with MINOS, installation would occur over two 10-hour shifts per day and four-day workweeks. The use of standard wood construction techniques and less highly trained technicians than required for MINOS, i.e., framers and laborers vs millwrights and welders, will result in a correspondingly adjusted wage scale.

To meet this installation rate an average of three truckloads of OSB and one truckload of scintillator must be delivered to the detector site each workday. We assume that these materials will be delivered to a separate receiving and pre-assembly building located at grade on the detector site. An ideal template for this is the MINOS surface building. This industrial building was built to specification by Breitung Township using a variety of local and economic development funds and leased to the project for the duration of the experiment with options for continued rental after construction. It is now used at the CDMS control room, and an auxiliary control room for MINOS. It is pictured in Figure 6.1. After our use is complete the township hopes to attract a new company (and jobs) to this surface facility.



Figure 6.25 Views of the MINOS surface building

The floor space required for the Off-Axis assembly building is larger than for MINOS since pre-assembly will be done here instead of in the main detector hall. Preliminary layout work indicated that a total working space of 35,000 sq.ft. will be required, or roughly 5 times the area of the MINOS surface building.

The OSB arrives on trucks in billets pre-cut to size. The scintillator modules arrive in reusable shipping containers. Both of these

loads are removed from the truck via a fork truck (or bridge crane). Two crews of four are used to receive materials and build stacks. After the stacks have been constructed they are transported a short distance to the below grade detector hall. In the hall they can be stacked near the construction face installed as delivered. The detector stacks are rigged using commercial articulated vacuum fixtures similar to the ones used for staging the MINOS steel plates (as shown in figure 6.2).

These fixtures can pick a load from the horizontal, rotate it to vertical, rig, and then release. The loads on the stacks, and the porous surfaces have been examined and

found to be well within the specifications for standard off-the shelf vacuum systems. Two different fixtures would be needed, one for rotating into each of the two views.



Figure 6.26

After the stack is picked, it is rigged into place with a crane. Once in place, two people (who run tag lines for rigging the stack) use two scissor lifts to move the length of the stack, securing it to the adjacent stack and the previous plane using construction screws delivered by collated screw driving systems. At the same time, the other member of the team is surveying the unit from one of the scissor lifts. After securing the stack, the crew returns to the location of the next stack . Along the way they will use the surveys from the previous

plane to correct it to vertical by attaching wood shims with screws. This operation is repeated 12 times each shift to install a plane.

After the plane is installed, a crew of two technicians installs the photodetectors, electronics, and cables up the units. Shift physicists then commission the planes.

The construction manpower required for installation (both shifts summed):

16	Receivers & brick builders (4 crews of 4)
8	Stack installers (2 crews of 4)
<u>4</u>	<u>QA / cablers</u>
28	Total installation crew

This is comparable to the 25 people used in constructing the MINOS planes. In addition to the installation staff and additional 6 support staff (supervision, safety, administration, network, telecomm, & janitorial) are required. Thus, a total staff of 34 is needed on site for construction of this detector.